QUANTITATIVE NMR IMAGING AND ITS APPLICATIONS *IN VIVO*

by

WENDY ANNE STEWART

B.Sc., University of Dundee, 1982

A THESIS SUBMITTED IN PARTIAL FULFILLMENT OF

THE REQUIREMENTS FOR THE DEGREE OF

MASTER OF SCIENCE

in

THE FACULTY OF GRADUATE STUDIES

(Department of Chemistry)

We accept this thesis as conforming

to the required standard.

THE UNIVERSITY OF BRITISH COLUMBIA

NOVEMBER, 1985

In presenting this thesis in partial fulfilment of the requirements for an advanced degree at the University of British Columbia, I agree that the Library shall make it freely available for reference and study. I further agree that permission for extensive copying of this thesis for scholarly purposes may be granted by the head of my department or by his or her representatives. It is understood that copying or publication of this thesis for financial gain shall not be allowed without my written permission.

Department of CHEMISTRY

The University of British Columbia
2075 Wesbrook Place
Vancouver, Canada
V6T 1W5

Date 14th April /86

ABSTRACT

The problem of quantifying NMR parameters, measured at a field strength of 0.15 Tesla using a whole body imaging instrument, and their potential use *in vivo*, have been investigated.

The spin-lattice relaxation times (T_1) of water doped with various concentrations of paramagnetic species were determined using the inversion-recovery method. Intensity was measured directly from images as a function of tau and T_1 obtained from a three parameter exponential fit of the data. The effects of varying imaging conditions on the values of T_1 obtained, were also examined. The results were compared with T_1 values obtained using a two-point computational method which is available on many commercial imaging instruments. This involves taking the ratio of an inversion-recovery image and a spin-echo image, which eliminates the dependence of the images on the equilibrium magnetization and the repeat time. The spin-spin relaxation times (T_2) were determined using the spin-echo method, of water doped with the same concentrations of paramagnetic species used to study T_1. Intensities were again obtained directly from images as a function of 2 tau and T_2 obtained from a two parameter exponential fit of the data. The effects of diffusion on the values of T_2 obtained were also examined. The values were compared with those obtained from

a two-point computational method, which takes the ratio of two spin-echo images with different tau-times. The T_1 and T_2 data were also compared with literature values obtained under conventional spectroscopic conditions, with no magnetic field gradients present.

The results of these studies, which compare favourably with those in the literature, have shown that it is possible to obtain reproducible values of T_1 in the range 100-600 ms, with acceptable errors (±12%) under variable imaging conditions. Reproducible values of T_2 can be obtained in the range 40-200 ms, which have errors of ±15% or less. Above this range the effects of diffusion become important.

Experimental allergic encephalomyelitis (EAE), an animal model for multiple sclerosis, was induced in a Macaca fascicularis monkey, and the development of the disease was followed using quantitative NMR imaging. This technique has been shown to be a powerful tool in the study of EAE in primates, since the progression of the disease is accompanied by changes in T_1 and T_2. The indications are that these changes will allow discrimination between areas of inflammation and others which contain demyelination.

CONTENTS

LIST OF TABLES

LIST OF FIGURES

LIST OF ABBREVIATIONS

ATP	adenosine triphosphate
B_o	static magnetic field
B_1	radiofrequency field
β	Bohr magneton
cm	centimetre
CT	computed tomography
$CuSO_4$	copper(II) sulphate
dB	decibels, measure of attenuation
^oC	degrees celcius
ΔB_o	static magnetic field inhomogeneity
ΔB_1	radiofrequency field inhomogeneity
ΔG	gradient non-linearity
D	diffusion coefficient
EAE	experimental allergic encephalomyelitis
FID	free induction decay
G_x	magnetic field gradient along the x-direction
G_y	magnetic field gradient along the y-direction
G_z	magnetic field gradient along the z-direction
GM	grey matter of the brain
γ	gamma, gyromagnetic ratio
Hz	hertz
I	nuclear spin
I_{IR}	intensity in an inversion-recovery image
I_{SE}	intensity in a spin-echo image

IR	inversion-recovery
mM	millimolar
mm	millimeter
$MnCl_2$	manganese(II) chloride
MS	multiple sclerosis
M_o	equilibrium magnetization
$M_{y'}$	magnetization in the xy plane
M_z	magnetization along the z-direction
ν	nu, Larmor precession frequency in hertz
NMR	nuclear magnetic resonance
ω	omega, Larmor precession frequency in radians per sec
^{31}P	phosphorous-31
%	percent
PET	positron emission tomography
RF	radiofrequency
ρ	rho, spin density
S	electron spin
τ	tau, the interpulse delay
τ_c	correlation time
T_1	spin-lattice relaxation time
T_2	spin-spin relaxation time
TR	repeat time, the time between successive reapplication of a pulse sequence
2DFT	two dimensional Fourier transformation
WM	white matter of the brain

GLOSSARY OF TERMS

Central nervous system: This consists of the brain and spinal cord.

Cerebral hemisphere: Either of the pair of structures constituting the main portion of the brain, occupying the upper part of the cranial cavity.

Demyelination: Destruction or removal of the myelin sheath of a nerve or nerves.

Encephalomyelitis: Inflammation involving both the brain and spinal cord.

Gross pathology: Diseased tissues visible to the naked eye.

Haemorrhagic necrosis: Death of tissue, usually as individual cells, groups of cells or in small localized areas, due to rupturing of blood vessels.

Histology: That department of anatomy, which deals with the minute structure, composition and function of the tissues. Histopathology: the histology of diseased tissue.

Inflammation: A localized protective response elicited by injury or destruction of tissue, which serves to destroy, dilute, or wall off both the injurious agent and the injured tissue. Histologically, it involves a complex series of events which include dilation of arterioles, capillaries and venules, with increased permeability and blood flow.

Intradermal: Within the dermis, which is the outer layer of skin deep to the epidermis, consisting of a dense bed of vascular connective tissue.

Ketamine hydrochloride: Chemical name (±)-2-o-chlorophenyl-2-methylaminocyclohexanone hydrochloride. A non-barbiturate, rapid acting general anaesthetic which can be administered intravenously or intramuscularly.

Mycobacterium tuberculosis: Species of micro-organism which causes tuberculosis. The disease is characterized by the formation of tubercles and caseous necrosis in the tissues.

Myelin: The lipid substance forming a sheath around certain nerve fibers.

Neuron: Any of the conducting cells of the central nervous system. A typical neuron consists of a cell body, containing the nucleus and the surrounding cytoplasm; several short radiating processes known as dendrites, and one long process (axon) which terminates in twig-like branches, and may have branches along its course.

Rompun: Chemical name, 2-(2,6-dimethylphenylamino)-4H-5,6-dihydro-1,3-thiazine. Potent sedative, hypnotic. Can be administered intravenously or intramuscularly.

Synapse: The anatomical relation of one nerve cell to another; the region of junction between processes of two adjacent neurons, forming the place where a nervous impulse is transmitted from one neuron to another.

ACKNOWLEDGEMENTS

I would like to thank Professor L.D. Hall for his support and encouragement throughout this work.

I would also like to express my appreciation to Dr. D.W. Paty, for his support and enthusiasm throughout our collaborative research. Thanks also go to Mr. D. Aikins, whose engineering expertise has been invaluable, and to the Research and Development group at Picker International, Cleveland, Ohio, for their helpful discussions.

I give special thanks to Anneke Rees for typing this thesis, and for her patience and encouragement throughout its preparation.

Dedication

To Professor Roy Foster

INTRODUCTION

The phenomenon of nuclear magnetic resonance (NMR) was first discovered by Purcell and Bloch[1,2] in 1946, and is now an important analytical tool for both scientists and physicians.

NMR spectroscopy has been used by scientists in the elucidation of complex chemical structures, such as steroids and proteins, in reaction product characterization, and in the study of electron-donor-acceptor complexes, to name a few examples from organic chemistry.[3] With progressive technical improvements in NMR instrumentation, many biological studies have also become possible. In 1971, Damadian[4] carried out <u>in vitro</u> proton NMR studies on rat tissue, and demonstrated differences between the relaxation behaviour of the protons in normal and cancerous tissue. This provided the first evidence that NMR signals could be used to discriminate between normal and diseased states. In 1973, the application of NMR to medicine was extended when Moon and Richards[5] detected the intraerythrocytic ^{31}P resonances of 2,3-diphosphoglycerate and inorganic phosphate from blood. They also demonstrated that the intraerythrocytic pH could be deduced from a detailed study of the inorganic phosphate chemical shift.

In 1974, the work of Moon and Richards was extended by Henderson, Costello and Omachi[6], who also detected the ^{31}P resonances from adenosine triphosphate (ATP) in human

erythrocytes. In the same year, Hoult et al.[7] showed that the ^{31}P NMR signals from ATP, phosphocreatine and inorganic phosphate could be obtained from intact muscle samples. ATP is the key metabolite in virtually every energy transfer process in the body. Its regeneration involves both inorganic phosphate and phosphocreatine; therefore metabolism could be followed for the first time in vivo using ^{31}P NMR spectroscopy. In addition, since the technique is non-invasive and does not require ionizing radiation, metabolic disorders could be followed over time and the effects of therapy monitored[8,9]. Over the past decade a large number of in vivo spectroscopic studies have been carried out[10-13], and many more are in progress.[14]

Imaging Methods

1. Back Projection

In most conventional NMR experiments the sample under study is placed in a uniform static magnetic field, B_o, and the equilibrium magnetization in the z-direction is perturbed by application of a radiofrequency (RF) pulse at the resonance frequency of the appropriate nucleus[15]. This work is concerned with proton NMR. The resonance frequency is given by equation 1,

$$\omega_o = \gamma B_o \qquad (1)$$

where γ = gyromagnetic ratio of the proton.

The ability to obtain spatially encoded information using the NMR signals from a sample was first demonstrated by Lauterbur in 1973[16].

In the imaging experiment, magnetic field gradients are applied, resulting in frequency labelling of the sample with respect to distance along the direction of the applied gradient. If the applied gradient (G_x for example) is linear, then equation 1 becomes

$$\omega_x = \gamma B_o + \gamma_x G_x \qquad (2)$$

where ω_x is the resonance frequency of nuclei at position x during application of gradient G_x.

Consider a sample comprising two tubes containing the same solution (for example, water) placed in a static magnetic field, as shown in Figure 1. If a linear G_x gradient is applied during data acquisition after a 90^o RF pulse, then the Fourier transform[17] of the time domain signal has the form of the projection shown in Figure 1a; the water in the two tubes has different resonance frequencies corresponding to the positions of the tubes along the x-axis. Similarly, application of a gradient along the y-axis during data acquisition and subsequent Fourier transformation provides the projection shown in Figure 1b. Now the water in both tubes has the same resonance frequency, and a single profile is obtained with twice the intensity from a single tube. If linear

combinations of the x- and y-gradients are used, a simple effective linear gradient is obtained, and hence projections may be obtained at any angle with respect to the y-axis (for example, 45°, as shown in Figure 1c). Usually, 180 projections are obtained, with the composite gradient 'rotated' at 1° intervals. The Fourier transforms of each projection are then "filtered" and "back projection"[18] carried out to provide the final image.

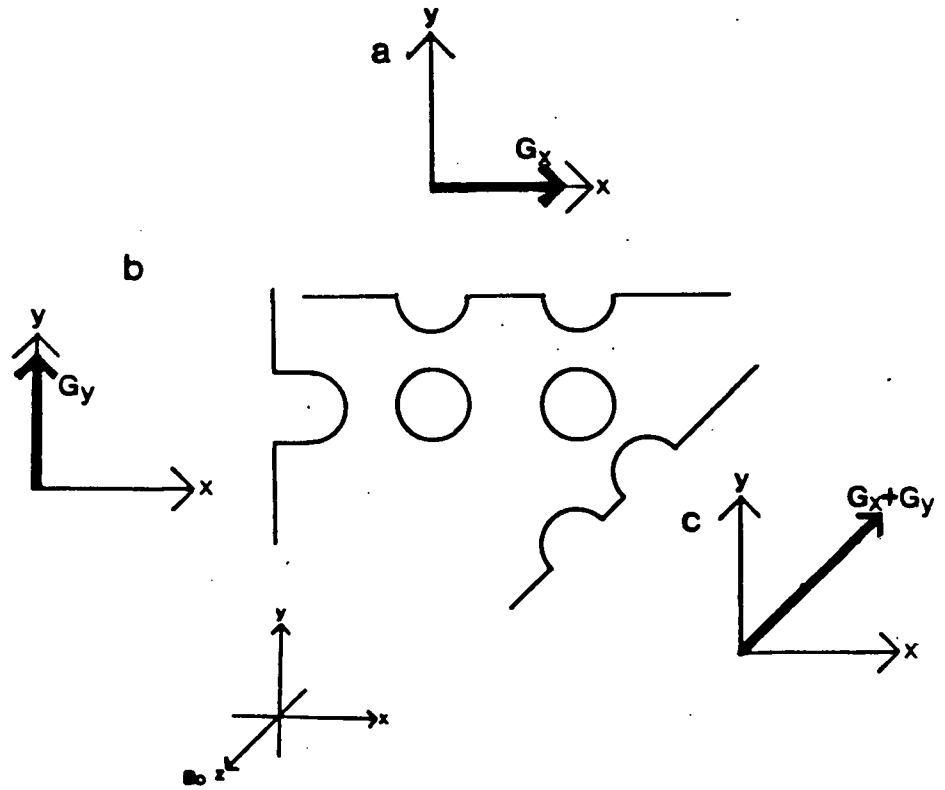

Figure 1: Single projections for back projection imaging.

a. Application of gradient G_x

b. Application of gradient G_y

c. Application of G_x plus G_y

2. Two-Dimensional Fourier Transformation (2DFT)

The idea of using Fourier methods in imaging was introduced by Kumar, Welti and Ernst in 1975[19]. 2DFT imaging is a specific example of a broader class of NMR techniques known as 2DFT spectroscopy[20]. An example of a pulse and gradient sequence used for 2DFT imaging is shown in Figure 2. If the imaging method of plane selection is used, the experiment begins with the application of a

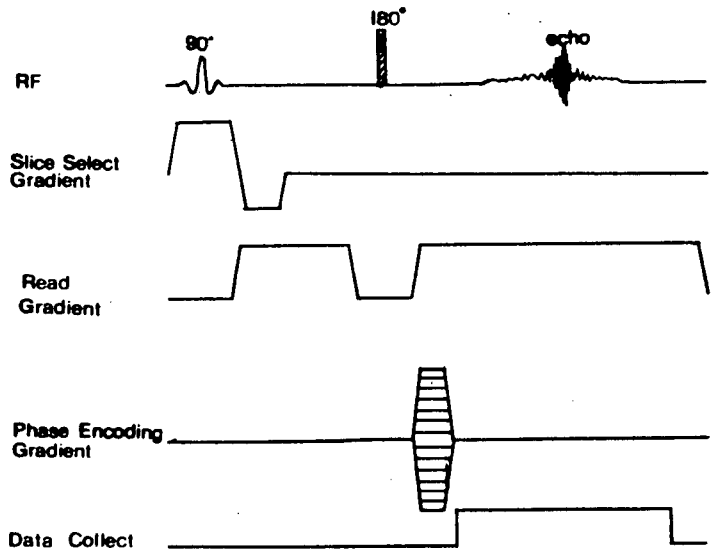

Figure 2: Two dimensional Fourier transform pulse and gradient sequence.

selective 90^{o} RF pulse together with a slice select gradient (see page 6 for description of slice selection).

During data acquisition, a "read" gradient is applied, which frequency-encodes the sample under study and thus provides spatial information; this functions in the same way as the gradients used in the Lauterbur method. In addition,

a phase encoding gradient is applied, perpendicular to the first, and its amplitude is incremented for each successive excitation. The number of these phase encoding increments chosen determines the 2D matrix size and thus the resolution (see Chapter 1). In all images obtained for this thesis, 256 phase encoding increments were used. The observed signal S(t) can be written as

$$S(t) = \int\int \rho(r) s(r,t) dxdy \qquad (3)$$

where s(r,t)dxdy is the contribution from the area dxdy, volume averaged over the slice thickness, at position r, and p(r) is the spin density. The area dxdy is referred to as a pixel. The 2DFT of S(t) is given by

$$S(\omega) = S(\omega_x, \omega_y) \qquad (4)$$

such that

$$S(\omega) = \int\int S(t) \exp(-i\omega t) dt_x dt_y \qquad (5)$$

For further details, the reader is referred to Mansfield and Morris[21].

Imaging methods may also be divided into groups depending on whether they receive signal from one point at a time[22], from a line[23], or from the whole sample[24].

Slice Selection

The two imaging methods described above provide spatial discrimination along the x, y-axes of the object. For an object of finite length, the resultant image represents the

projection of all the spin-densities onto a nominal plane. Clearly, it is necessary to have a means for selecting a slice of known thickness at any position within the object.

This technique of selective excitation or slice selection was first proposed by Garroway, Grannell and Mansfield in 1974[25].

Consider the irradiation of a thin cross-sectional area perpendicular to the direction of the static magnetic field, B_o (Figure 3). If a linear magnetic field gradient is applied in the B_o direction, the absorption frequency is a function of position in this direction.[26] Irradiation with a pulse containing a narrow band of frequencies will then excite only the desired cross-section as shown in Figure 3.

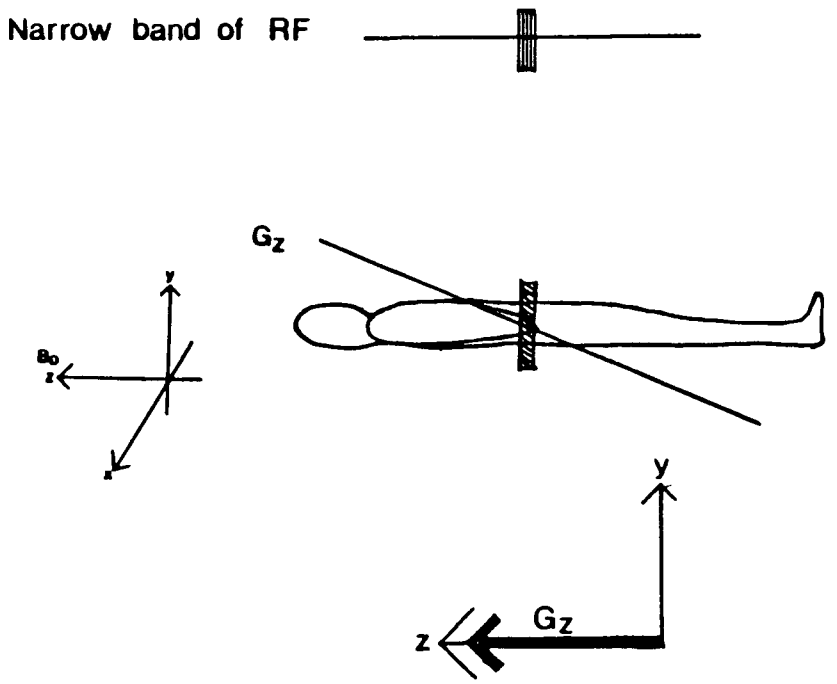

Figure 3: Slice selection in imaging.

It is desirable that the physical domain of the excited slice be rectangular in cross section. To implement this, a rectangular envelope of frequencies must be applied to the sample; in turn, this requires use of a sinc-shaped pulse in the time domain.

In practice, the sinc function must be truncated since it extends to infinity. The result of this is some distortion in the frequency-envelope. These distortions can be minimized by weighting the time domain with a damping function, typically a Gaussian function. The resulting RF pulse shape used for NMR imaging is shown in Figure 4, together with its Fourier transform.

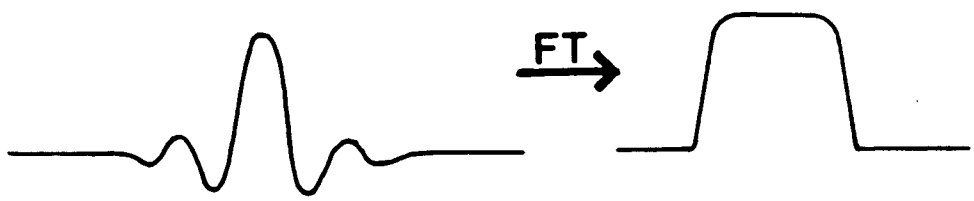

Figure 4: Selective radio-frequency pulse in the time domain and its Fourier transform.

The response of the nuclei within this slice can be described as follows. The effective field experienced by the nuclei (B_{eff}) is given by equation 6.

$$B_{eff} = B_1 + G_z Z \qquad (6)$$

In the absence of the gradient and assuming a sufficiently intense B_1, the nuclear moments would precess in phase. However, due to the presence of the gradient, nuclei at different positions along B_o will experience different local fields. This results in a loss of phase coherence at the end of the 90^o RF pulse. However, it can be shown for a 90^o RF pulse that this variation in phase with z is approximately linear, and thus phase coherence can be recovered by z-gradient reversal for a length of time approximately half that of the irradiating pulse. The full sequence of events for slice selection are shown in Figure 2. The slice thickness is determined by the magnitude of the magnetic field gradient used, and the frequency bandwidth of the selective RF pulse.

In December 1982, the prototype whole body NMR imaging system of Picker International was installed in the Extended Care Unit of the Health Sciences Centre Hospital on the University of British Columbia (UBC) campus. This system is part of the Imaging Research Centre, which also includes a CT X-ray scanner and Positron Emission Tomograph. The NMR imaging system consists of an Oxford Instruments superconducting magnet, with a room temperature bore of 1 metre, operating at a static magnetic field strength of 0.15 Tesla (proton resonance frequency, 6.4 MHz). The system is

interfaced with a Perkin Elmer computer, and all operational software is written by Picker International (see Appendix I for more details). Patient scanning for clinical research has been carried out on a volunteer basis, since NMR imaging systems have not yet been approved as diagnostic tools in Canada. Time has also been available for scientific research. The UBC instrument makes use of the imaging method of plane selection. The first software package available to the user only contained the technique of filtered back projection for obtaining an image; however subsequent packages also contained software for imaging using two-dimensional Fourier transformation.

A number of different pulse sequences are available for use on the Picker International system, for example:

1. Inversion-recovery

   (180^{o}-τ-90^{o}-Data acquisition-Delay-)n

For this sequence a 180^{o} RF pulse is used to invert the equilibrium magnetization, M_o, along the z-axis to the -z-direction, i.e. $M_z = -M_o$. Spin-lattice relaxation then takes place and the magnetization along z is gradually restored to M_o (see Figure 5). Application of a 90^{o} RF pulse at time tau (τ) after the 180^{o} pulse will then tip any magnetization along z into the x'y' plane, which will induce a signal in the receiver coil, the amplitude of which is given by equation 7.

$$I_{(\tau)} = I_o(1-2\exp(-\tau/T_1)) \qquad (7)$$

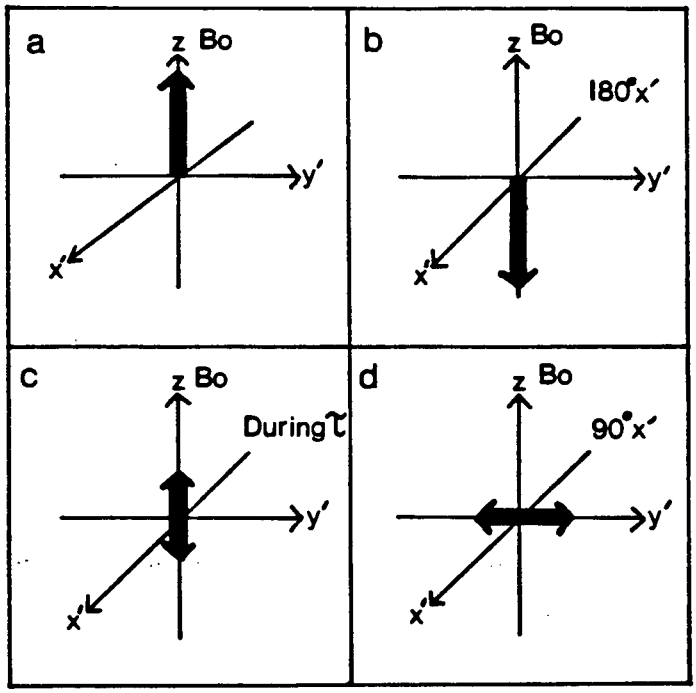

Figure 5: Vector diagrams demonstrating the effects of an inversion-recovery pulse sequence on a spin-system.

A plot of signal amplitude versus τ gives an exponential recovery curve like that shown in Figure 6. The return of the magnetization to its equilibrium state is dependent on the spin-lattice relaxation time, T_1. The magnetic interactions giving rise to this relaxation are considered in more detail in Chapter 2.

The actual inversion-recovery pulse sequence used on the whole body imaging system is given by equation 8.

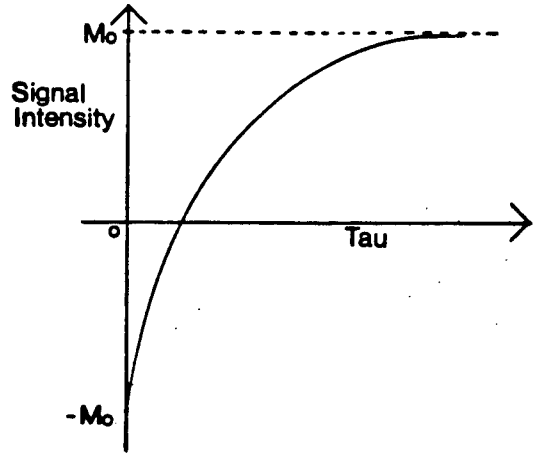

Figure 6: Plot of intensity versus tau, the inter-pulse delay, for an inversion-recovery pulse sequence.

$$(-180°-\tau-90°-t-180-t-\text{Data aquisition}-)_n \qquad (8)$$

The reasons for having the second 180^o RF pulse and its implications are dealt with in Chapter 2.

2. Spin-echo $(90^o-\tau-180^o-\tau-$Data Acquisition-Delay$-)n$

At this juncture it seems appropriate to introduce the concept of the spin-echo[27]. It will also be considered again in Chapter 2.

The use of this pulse sequence is more clearly understood by considering the vector diagrams in Figure 7. After the 90^o RF pulse (along x'in the rotating frame of reference) the magnetization M_o is turned into the x'y' plane along y'. i.e. the individual protons precess about z

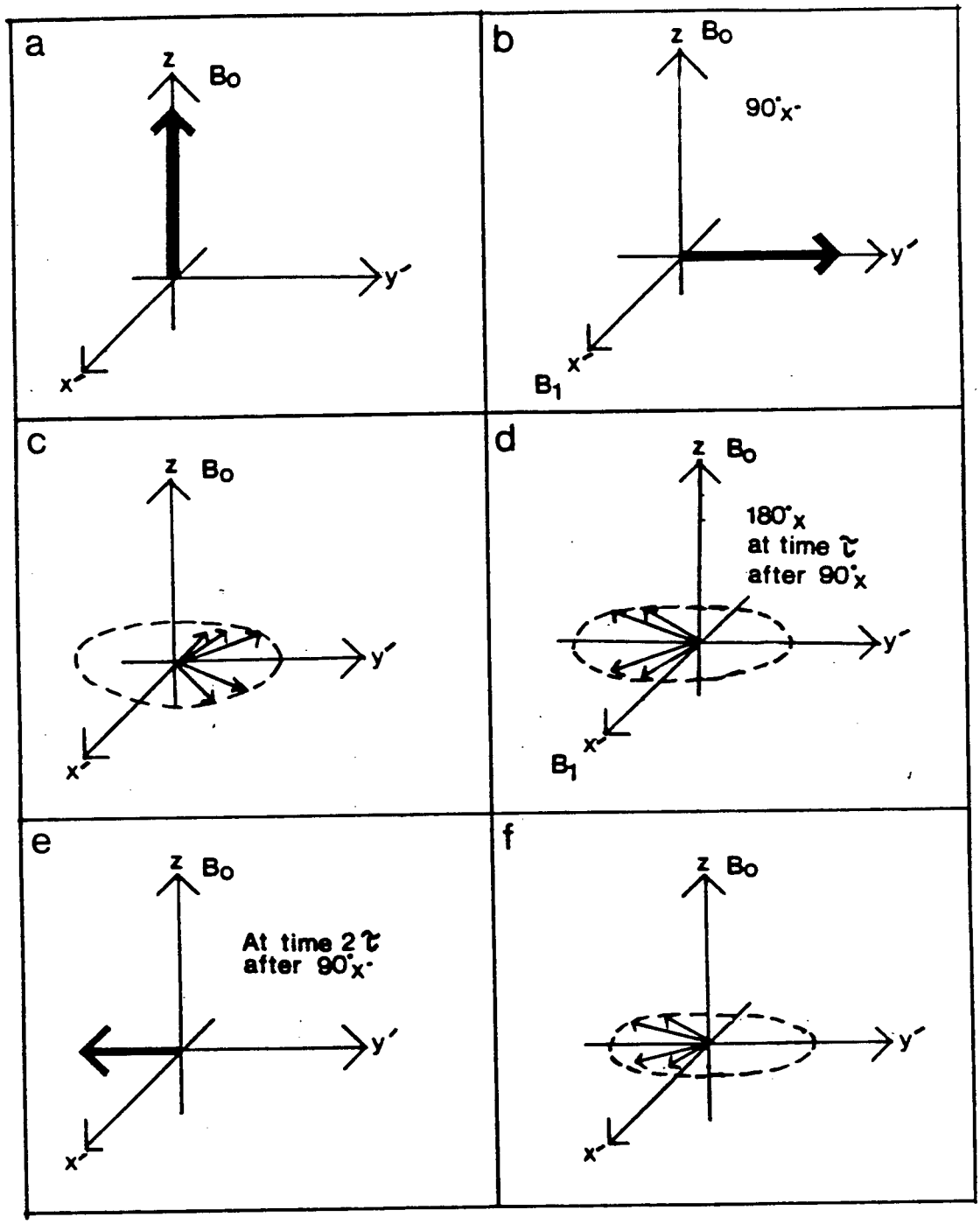

Figure 7: Spin-echo pulse sequence. Schematic diagrams showing formation of the echo.

in the xy plane of the laboratory frame of reference (Figure 7b). The protons then dephase relative to each other due to the magnetic field inhomogeneities and spin-spin relaxation. Some protons will precess faster than ω_o and some slower (Figure 7c). The spin-spin relaxation time, T_2, describes the phase memory of the spin system and hence the decay of magnetization in a particular direction in the x'y' plane after application of the 90^o RF pulse. If a 180^o RF pulse is applied along x' at a time τ after the 90^o pulse, the protons will now be rotated 180^o about x' and those that were rotating clockwise in the x'y' plane will rotate counterclockwise and vice versa (Figure 7d). A further time τ after the 180^o pulse, the individual protons will cross the -y' axis together, and a negative signal will build up and decay in the receiver coil (this is the "echo"), after this the protons will continue to dephase. The inverting 180^o pulse cancels out any static magnetic field inhomogeneity effects and in this way the amplitude of the spin-echo is dependent only on T_2 and τ. The amplitude of the spin-echo for a given τ-value is shown in equation 9.

$$I_{(2\tau)} = I_o \exp(-2\tau/T_2) \qquad (9)$$

If, however, molecular diffusion takes place between the 90^o and 180^o pulses, then the echo amplitude will be affected by the different magnetic fields[28] experienced by individual protons as they move. The echo amplitude is then given by equation 10,

$$I_{(2\tau)} = I_o \exp(-2\tau/T_2) \exp\left(-\frac{2}{3}\gamma^2 G^2 D\tau^3\right) \qquad (10)$$

where G is the spatial magnetic field gradient and D is the diffusion coefficient. In the absence of the effects of diffusion, a plot of echo amplitude versus 2τ gives an exponential plot like that shown in Figure 8.

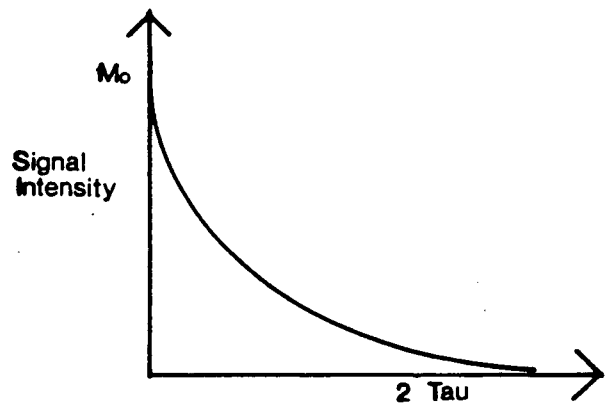

Figure 8: Plot of intensity versus 2 tau for a spin-echo pulse sequence.

3. Free Induction Decay (90^o-Data acquisition-Delay-)n

In this pulse sequence, after the 90^o RF pulse the equilibrium magnetization, M_o, is turned into the x'y' plane and sampled almost immediately. The signal amplitude is given by equation 11.

$$I = I_o (1-\exp(-TR/T_1)) \qquad (11)$$

For all three pulse sequences described above, the time between successive reapplications of the entire sequence is referred to as the repeat time (TR).

The appearance of the NMR image is dependent on a number of parameters of the object; namely, spin-lattice relaxation time (T_1), spin-spin relaxation time (T_2), spin-density (ρ), diffusion (D) and flow. It also depends on the pulse sequence used to obtain the image, which is chosen to provide an image in which the displayed intensity is weighted towards one of the object parameters. For example, the inversion-recovery pulse sequence provides an image which is T_1 weighted[29], and the contrast observed between different areas of the object is mainly due to the difference in their T_1-values. This can be explained as follows: for a given τ-value, areas of different T_1 will have recovered different magnitudes of z-magnetization: thus when the 90° sampling pulse is applied to observe the signals, areas of different T_1 will have different intensity. As a second example, the Free Induction Decay sequence provides an image which is mainly dependent on the spin density[30], ρ, or in other words, the number of protons present in any part of the sample. This is easily explained, since this sequence merely samples the equilibrium z-magnetization. However, if the delay between data acquisition and reapplication of the 90° pulse is not sufficiently long for all protons to relax back to

equilibrium, then the image will also display some degree of T_1 dependence. Spin-spin relaxation may also occur between the 90^{o} pulse and data acquisition, resulting in an image which also has a dependence on T_2.

In vivo NMR images can now be obtained with exquisite anatomical detail (Figure 9). With this achieved, the next

Figure 9: Sagittal image of a human head obtained using a spin-echo pulse sequence.

goal is to quantify NMR parameters measured in vivo, in the hope that they can provide a method of tissue characterization[31,32]. In addition, it is only with the help of quantitative measurements that there is any chance of differentiating between different types of pathology which appear visually identical on the NMR image.

Thesis Objectives

1. To determine whether it is possible to obtain values of the spin-lattice relaxation time, which are reproducible and have acceptable errors, under the conditions of the imaging experiment. The effects of varying the imaging conditions on the values obtained will also be examined.

2. To determine whether it is possible to obtain values of the spin-spin relaxation time, which are reproducible and have acceptable errors, under the conditions of the imaging experiment.

3. To apply quantitative NMR imaging in vivo and determine whether it is feasible to use the spin-lattice and spin-spin relaxation times to differentiate between pathology which appears visually similar on the NMR image.

In addition to the usual problems of quantitative NMR measurements, the conditions of the imaging experiment introduce further possible sources of error, namely:

1. Inhomogeneity of the static magnetic field (B_o) and the RF field (B_1). In imaging, the use of large bore magnets means that field inhomogeneities are difficult to overcome. If these inhomogeneities are large, they would give rise to a range of relaxation times, since they are field dependent.[33]

2. Magnetic field gradient non-linearity. This causes distortion in the image.

3. Slice selection. This introduces the problem of volume averaging which is discussed in detail in Chapter 2.

4. Spatial resolution. This will determine the smallest area which can be studied.

5. Reproducibility. If quantitative measurements are to be of diagnostic use they must be reproducible over time.

6. Methods of Reconstruction. These can affect the appearance of the image and introduce ambiguities in the observed intensities.

7. Software Limitations. Certain parameters (such as TR) have limits, which can affect the outcome of accurate quantitative measurements.

At the outset, the strategy of this work was to carry out quantitative measurements on simple systems, then progress to more complex ones. This proved to be an unexpectedly difficult task. Initially, much time was expended to obtain spacially encoded 'spectra' using Fourier transformation of single projections from back projection data sets (Figure 10) of vials containing water doped with various concentrations of copper(II) sulphate ($CuSO_4$). The intention was that the signal intensities from these 'spectra' could be used for calculation of T_1, without artefacts from any subsequent imaging operation. It was expected that if the inversion-recovery pulse sequence was used, then, as described earlier, positive and negative signal intensities would be observed, depending on the

Figure 10: Fourier transform of a single projection in back projection imaging.

relaxation time of the sample under study and the choice of τ-value. However, when in practice a single concentration was studied using a range of τ-values, the observed signal intensities were always found to be positive. This implied that the absolute sign of signal intensities around the null point was in serious doubt, and could affect the value of T_1 obtained. In addition, when sets of different solutions were studied simultaneously, fluctuations in signal signs for individual solutions were observed and phase errors were apparent. An example is shown in Figure 11. In an attempt to understand these phenomena, which the manufacturers, Picker International, could not explain, various combinations of solutions doped with $CuSO_4$ were studied. It became apparent that the phenomena arose from the methods of phasing and reconstruction employed by Picker International. These problems are considered in detail in Chapter 1. That chapter also evaluates some of the other sources of error

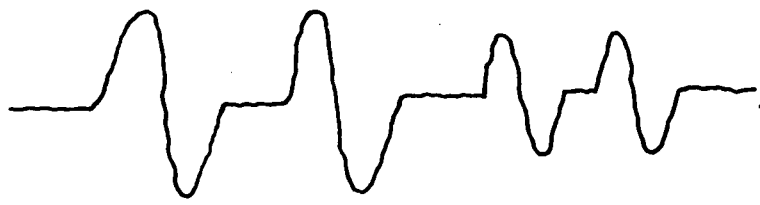

Figure 11: Fourier transform of a single projection in back projection imaging showing phase errors.

mentioned previously, such as B_o inhomogeneity, using phantoms containing water doped with paramagnetic ions.

Once the behaviour of the instrument was understood, quantitative T_1 and T_2 measurements were carried out on these simple systems. The effect of the imaging conditions on the values obtained was studied, and complete error analyses carried out on all the results.

The ultimate goal of the studies was, of course, quantitative applications in vivo. The ability to carry out quantitative NMR measurements in vivo is a difficult task. There are a number of reasons for this:

1. The mammalian cell composition and environment is very complex and is not static.

2. Water exists in more than one state within cells[34], and if there is slow exchange on the NMR time scale, contributions may come from each separate state giving rise

contributions may come from each separate state giving rise to multiexponential relaxation behaviour[35]. This means that the resultant signal intensity can be the sum of signal intensities from the various compartments having different relaxation properties. This is considered in more detail in Chapter 2.

3. Mobile fat protons may contribute to the NMR signal, again giving rise to multiexponential relaxation behaviour since the protons of fat and water typically have different relaxation rates, but virtually identical resonance frequencies at the low magnetic field strength used in imaging.

These obstacles present a real challenge. Chapter 3 describes the first use of quantitative NMR imaging to study the development of Experimental Allergic Encephalomyelitis (EAE), a well documented[36] animal model for Multiple Sclerosis (MS)[37], in primates. EAE was induced in a Macaca fascicularis monkey, and the development of the disease was followed using quantitative NMR imaging. The disease gives rise to abnormal areas in the central nervous system (CNS) which are similar to those observed in humans with MS. These abnormal areas appear bright on a spin-echo image[38] and dark on an inversion-recovery image[39], due to the elevation in their T_2 and T_1 values respectively. Quantitative measurements were carried out on the monkey's brain from the day of detection of the disease until death.

mortem, and the T_1 and T_2 values. These studies have already shown NMR imaging to be a powerful tool in the study of EAE in primates, and the future looks promising for extrapolating the findings to the study of MS in humans.

CHAPTER 1

EVALUATION OF THE INSTRUMENT

In preparation for carrying out quantitative NMR measurements on the whole body NMR imaging instrument, it is important that its mode of operation be fully understood; the following evaluation provided the necessary information for measuring the NMR parameters of interest in this work.

The effects of field inhomogeneity on the quality of images obtained using the instrument were examined. This provided a numerical value for the homogeneous volume at the centre of the magnet. Within this volume, the smallest object which could be identified was then determined. This is referred to as the spatial resolution. The effects of automatic setting of the attenuator, and the methods of phasing and reconstruction used on the instrument were studied. The problems they introduced were identified and explained, thereby allowing useful quantitative measurements to be carried out on this instrument. This chapter describes the process of evaluation in detail.

a. Static Magnetic Field Inhomogeneity and Radiofrequency Field Inhomogeneity

The usual method adopted for studying the spatial distribution of these fields involves plotting them on a

point by point basis, which is time consuming. It was therefore decided to construct phantoms which could provide an indication of the distribution of the static magnetic field inhomogeneity, ΔB_0, and the radiofrequency field inhomogeneity, ΔB_1. These phantoms consisted of equally spaced 1 cm diameter glass tubes containing water doped with $CuSO_4$, as shown in Figure 12. Using the instrument

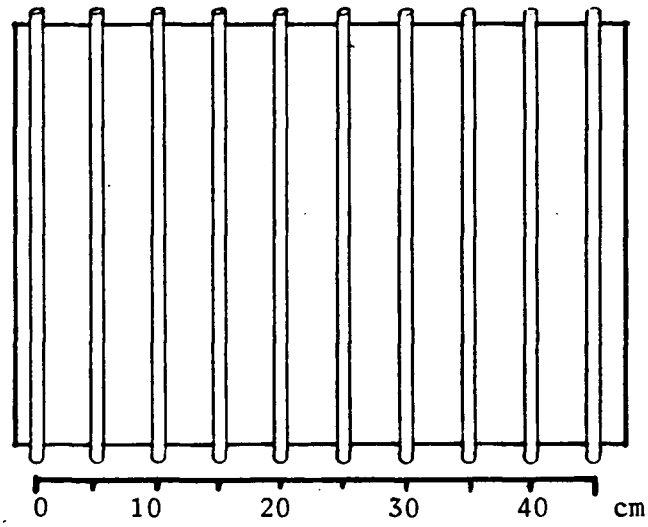

Figure 12: Diagram of parallel tube phantom for studying magnetic field inhomogeneity.

transmitter coil, which is also used for body imaging, 10 mm and 20 mm slice images were obtained using the Free Induction Decay sequence (FID) shown in Figure 13. Images were obtained in all three orientations, xy, xz and yz, using a 256 x 256 data matrix. An example of these images, taken in the xz plane, is shown in Figure 14. Distortions

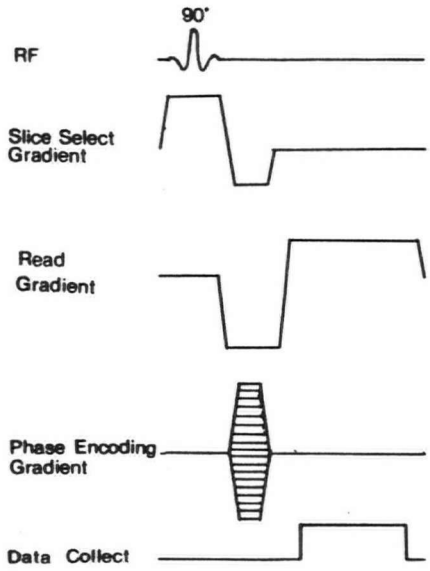

Figure 13: Free Induction Decay (FID) pulse and gradient sequence.

in the images of the glass tubes represent ΔB_0 and/or gradient non-linearity, ΔG. The distortions are observed on

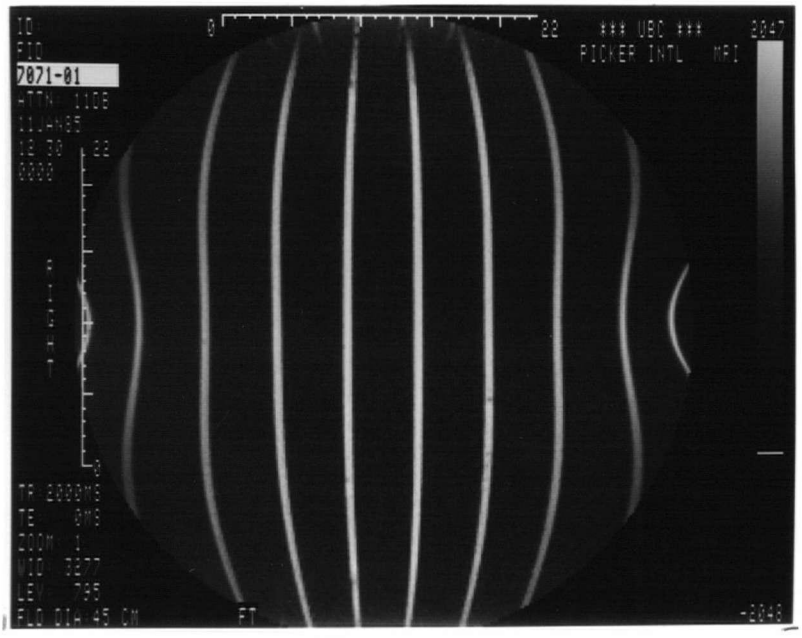

Figure 14: FID image of parallel tube phantom in the xz plane.

the periphery of the image which shows that, as expected, ΔG and ΔB_o become significantly larger as one moves away from the coil centre. Variation in the intensity across the image provides information on ΔB_1. Imperfect pulses will result in a variation in intensity in that region of the image. Figure 15 is a plot of intensity as a function of distance along the x-direction; it demonstrates clearly how the intensity varies.

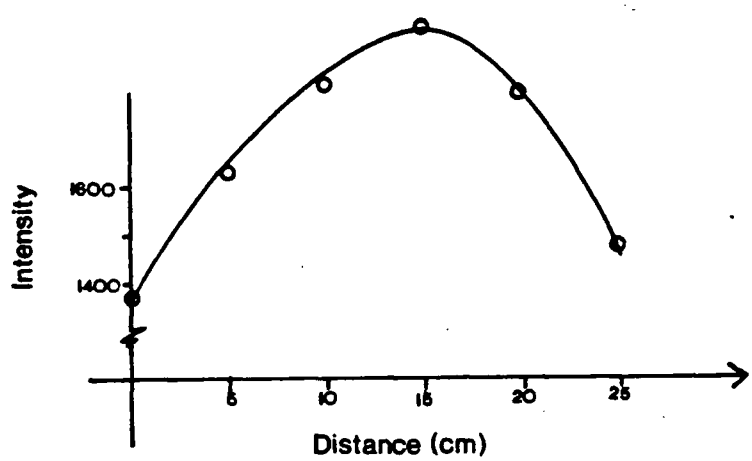

Figure 15: Plot of intensity as a function of distance along the x-direction.

Examination of all these images together indicates that a volume of 12100 cm^3 at the centre of the coil is homogeneous, and should provide good quality images and consistent quantitative measurements. Variations in pulse length across this region can be corrected for in the data processing. Outside this region the homogeneity

deteriorates, and although qualitatively useful images can be obtained out to 45 cm in diameter and of 45 cm along the magnet axis, intensity and spatial distortions are both prevalent.

b. Spatial Resolution

A simple phantom was constructed to determine the spatial resolution of the instrument used. It consisted of

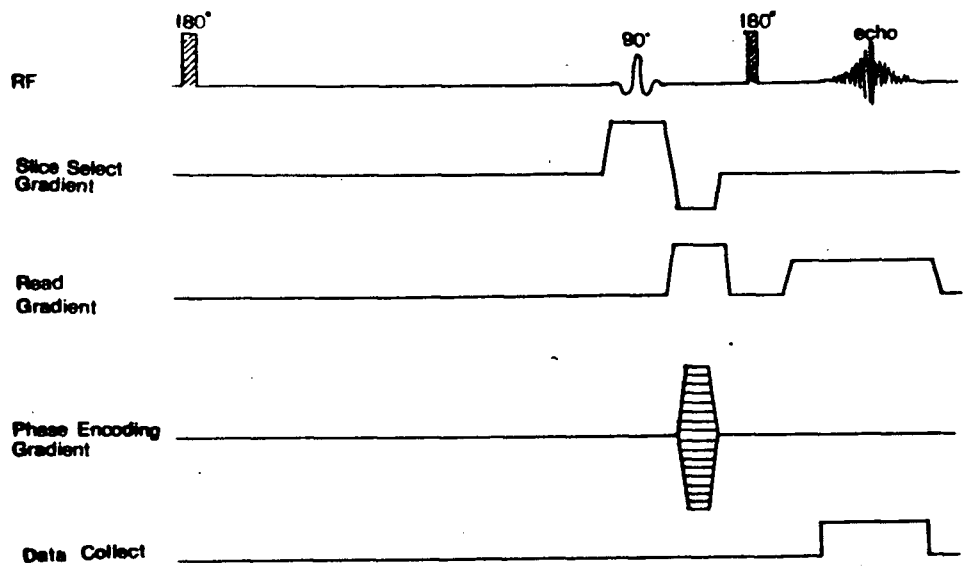

Figure 16: Inversion-recovery pulse and gradient sequence.

melting-point capillary tubes filled with two different solutions of $CuSO_4$, 0.99 mM and 2.54 mM, randomly arranged in vials of 2 cm diameter. 10 mm horizontal slice images were then obtained using the inversion-recovery sequence given in Figure 16. As can be seen in the image in Figure

17, it appears that individual capillary tubes can be identified which suggests that 1 mm resolution is

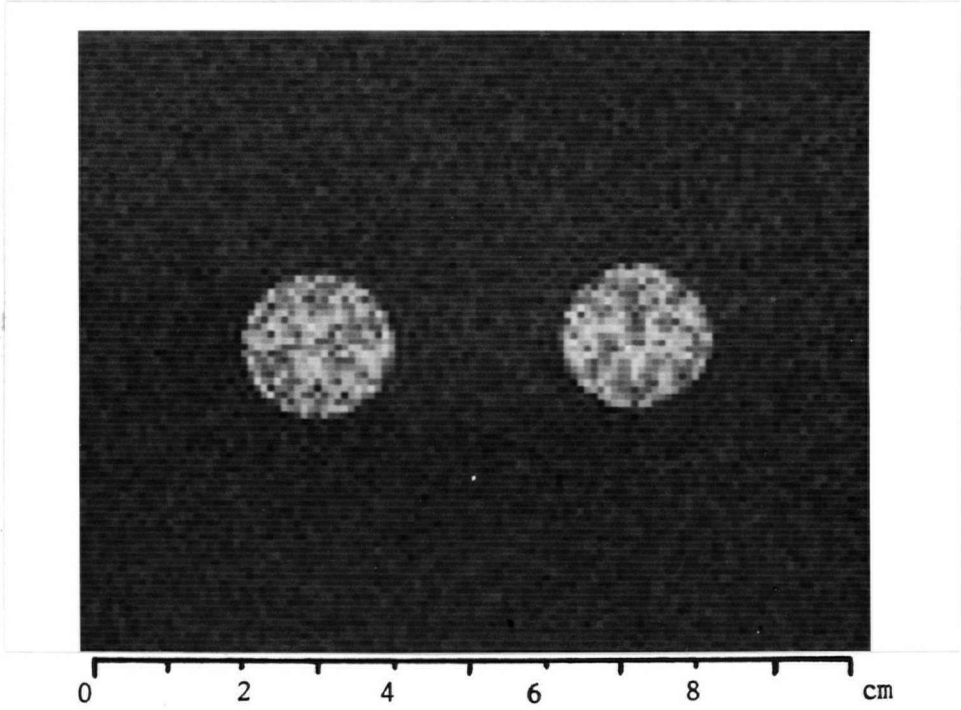

Figure 17: Inversion-recovery image of capillary tube phantom.

attainable. However, it is possible that the signal intensity observed in a single pixel is arising from more than one tube. A second phantom was therefore constructed, and is shown in Figure 18; all dimensions are as indicated.

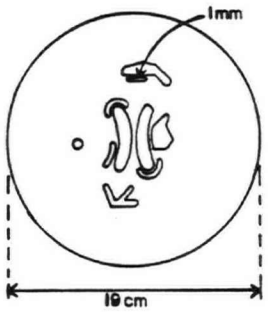

Figure 18: Diagram of resolution phantom.

In the image shown in Figure 19, the arrow indicates the resolution of the 1 mm perspex wall between two of the

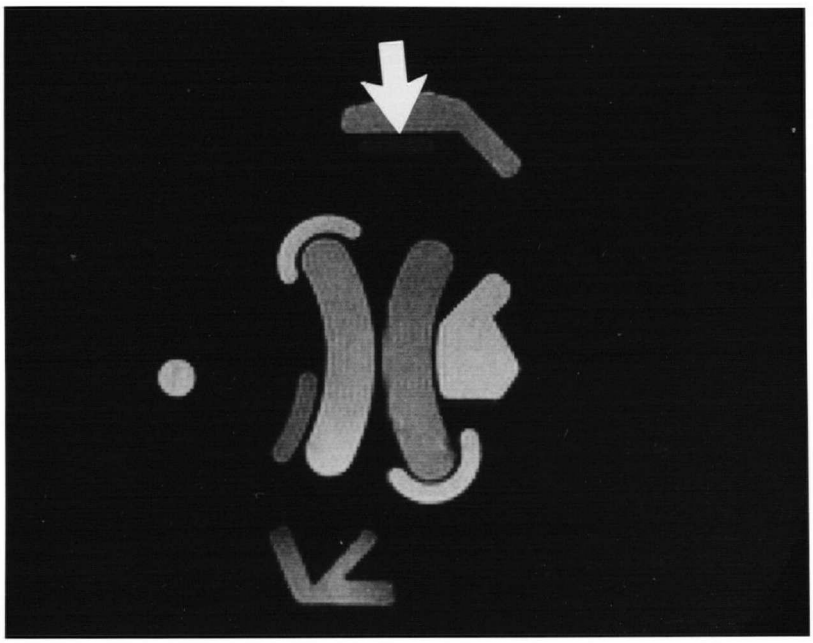

Figure 19: Spin-echo image of resolution phantom.

areas. This demonstrates that 1 mm is indeed easily resolvable and the maximum resolution possible is somewhat less than this.

c. Attenuation

The instrument used in these studies is designed such that it automatically changes the input gain of the RF receiver in order to maximize the signal to be digitized. This implies that for a series of inversion-recovery images with a range of τ-values (where τ = pulse interval), the

attenuation will not be constant and the intensities not directly comparable. The instrument, however, also allows manual setting of the attenuator. For all studies in this thesis, the attenuation was set based on the signal from the

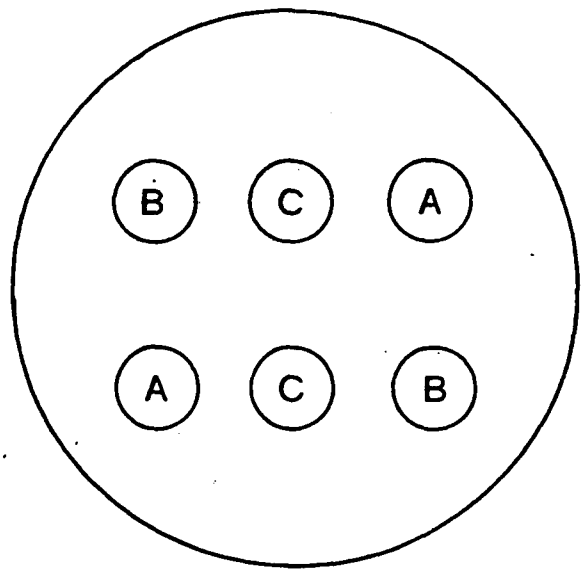

Figure 20: Phantom used for studying attenuation and for carrying out T_1 and T_2 measurements.

sample using a spin-echo sequence with 2τ = 26 ms and TR = 5 sec.

In order to check whether manual setting of the attenuation provides the same intensities as automatic setting, a simple experiment was carried out. The phantom shown in Figure 20, which contained three solutions of $CuSO_4$, was placed in the receiver coil and two images obtained using the spin-echo sequence with 2τ = 26 ms and TR = 5 sec. The first image was obtained with automatic setting of the attenuator, which gave 26 decibels (dB). The

second image was then obtained by manually setting the attenuation to 26 dB. The intensities obtained for each solution are given in Table I.

Table I: Intensities from two spin-echo images comparing manual and automatic setting of the attenuation. Intensities are given as the mean values from 2.6 cm^2 plus or minus standard deviation, at the centre of the vials. Two values are given for each solution corresponding to two different positions in the receiver coil.

Attenuation	4.96 mM		2.54 mM		0.99 mM	
Automatic	123 ± 7.6	133 ± 6.1	140 ± 6.5	134 ± 6.5	154 ± 7.4	146 ± 9.7
Manual	122 ± 7.6	131 ± 5.9	139 ± 6.6	133 ± 6.5	152 ± 7.6	145 ± 7.9

The intensities observed in both images are virtually identical. It can therefore be assumed that manual setting of the attenuation will provide images with the correct intensities.

d. Phasing and Reconstruction

As previously considered, the contrast observed in images of an object which has regions of different T_1 values, obtained using the inversion-recovery (IR) pulse sequence 12, is dependent on the intrinsic difference

$$(-180°-\tau-90°-\text{Data acquisition}-)_n \qquad (12)$$

between the spin-lattice relaxation rates of the protons within the different spatial domains. This leads to intensity changes which are a function of the pulse interval, τ. A typical situation for a two compartment sample is shown in Figure 21 for two solutions of $CuSO_4$ (see Chapter 2). The signal intensity observed from a single compartment at a particular value of τ is given by equation 13:[40]

$$I_\tau = I_0\{1-[1+W(1-\exp(-k/T_1)]\exp(-\tau/T_1)\} \qquad (13)$$

where I_0 = intensity at $\tau >> T_1$

k = waiting period between data acquisition and reapplication of the 180° pulse

W = correction factor for 180° pulse.

Although the NMR data-acquisition itself produces signals which have the phase information necessary to distinguish between the positive and negative-going signals associated with the magnetization plot shown in Figure 21a, many imaging protocols can only produce NMR signals in the "absolute mode". What this means is that after acquisition of the time domain signal and subsequent Fourier transformation, all signals are rectified to become positive. In those circumstances, the form of the

inversion-recovery intensity curve corresponds to Figure

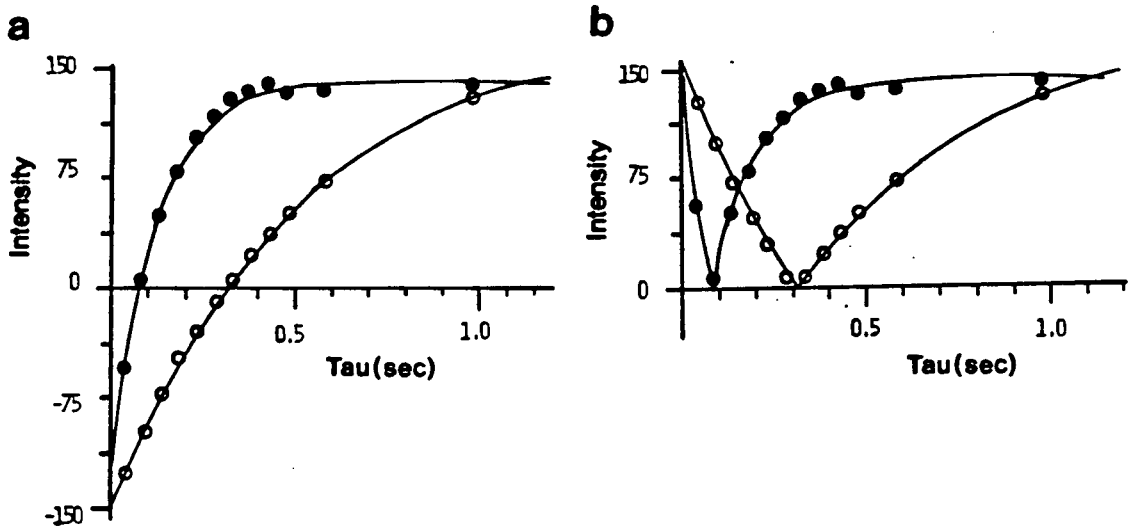

Figure 21: a. Plot of intensity versus tau for ● 4.96 mM and ○ 0.99 mM $CuSO_4$.

b. Plot of intensity versus tau for ● 4.96 mM and ○ 0.99 mM $CuSO_4$, with magnitude reconstruction.

21b, and the 'high intensity' signals observed in a reconstructed image could equally well come from a region of long T_1 as from one of short T_1. In order to minimize the occurrence of this ambiguity, the software of the instrument used in this study has the option of "real-intensity" reconstruction, which provides either positive or negative numbers, as appropriate, when an IR pulse sequence is employed. However, during attempts to obtain values of T_1 from various systems, it was observed that this method of reconstruction introduced additional problems.

In order to illustrate the phenomenon observed, two simple phantoms were constructed, each consisting of a 20 mm

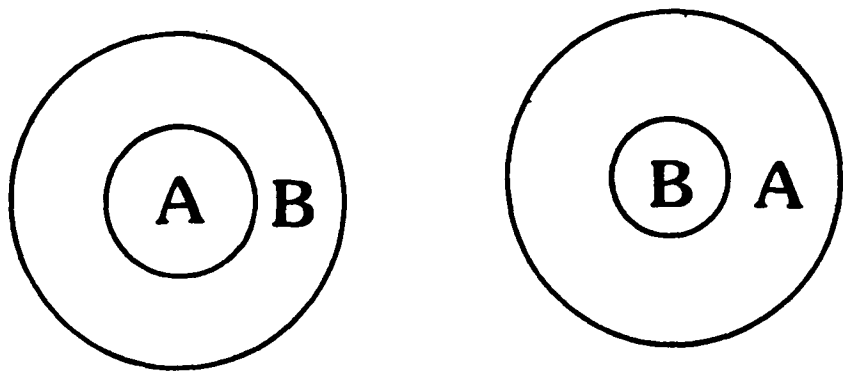

Figure 22: Phantom used for studying intensity ambiguities
A = 4.96 mM $CuSO_4$, B = 0.99 mM $CuSO_4$

diameter vial located inside a beaker of 70 mm diameter (Figure 22). The two aqueous solutions contained $CuSO_4.5H_2O$ at accurately known concentrations of 4.96 mM and 0.99 mM and having known T_1 values of 117 ms and 534 ms respectively (see p.60). As assembled, phantom-A corresponds to a 'hot-spot' and phantom-B to a 'cold-spot' in terms of relative T_1 values.

The two phantoms were placed side by side in the receiver coil used for head imaging, which has an aperture of 30 cm, and horizontal (xz) 10 mm thick slice-images were obtained simultaneously through both. IR images were

obtained with τ-values ranging from 50-1000 ms and TR of 4 sec plus τ. The resultant images are shown in Figure 23. The positions of the two phantoms were then reversed and the experiments repeated; as expected, the relative signal magnitudes of each particular solution were unchanged. The white horizontal line through each image shows the position of the cursor, and the trace below it, the corresponding intensity-projection. The intensity trace shows clearly the positive and negative-going signals, as can be seen in Figure 23c where the outer-component of the right-hand phantom and the inner component of the left-hand phantom are both negative.

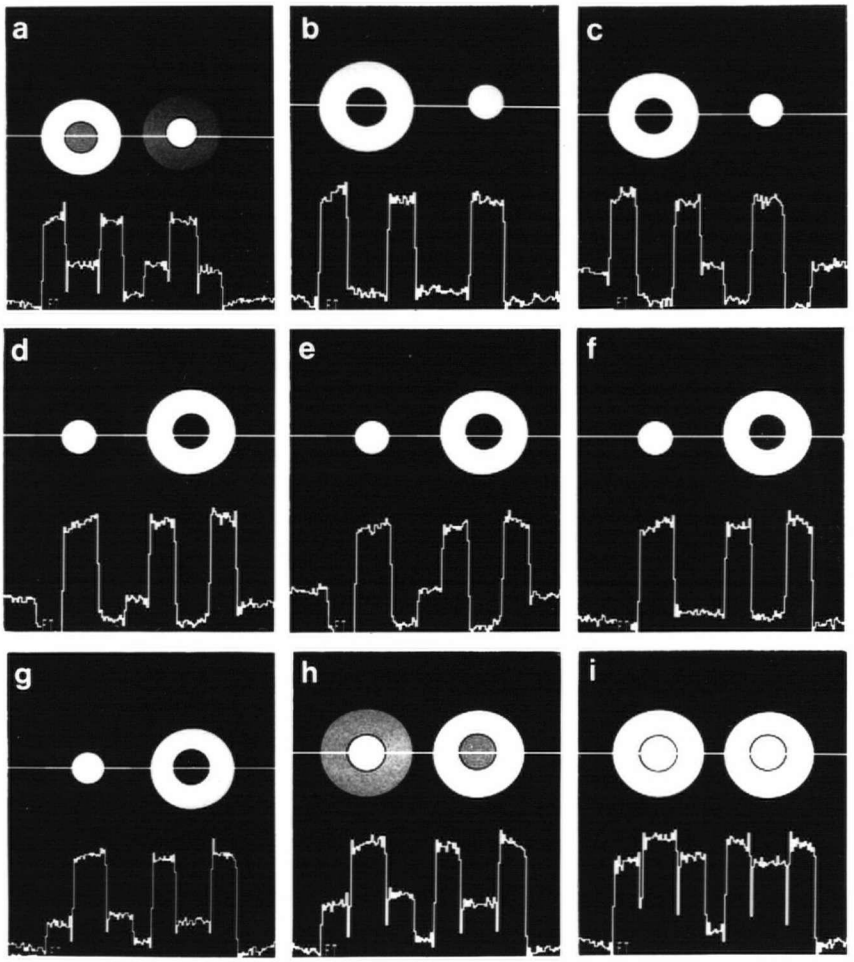

Figure 23: Inversion-recovery images demonstrating intensity ambiguities.

a. τ = 50 ms b. τ = 100 ms
c. τ = 150 ms d. τ = 250 ms
e. τ = 300 ms f. τ = 400 ms
g. τ = 500 ms h. τ = 600 ms
i. τ = 1000 ms

Since phase-sensitive reconstruction was employed to obtain the IR-images in Figure 23, one would expect the relative intensities of each of the two solutions to follow the trend shown in Figure 21a; however, as can be seen both from the cursor traces themselves and the plot of intensity versus τ shown in Figure 24, this is not the

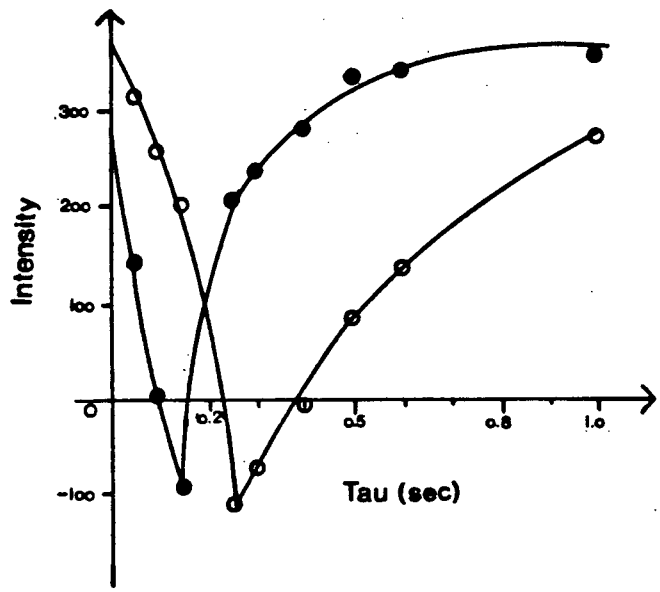

Figure 24: Plot of intensity versus tau showing fluctuations in signal sign.
● 4.99 mM $CuSO_4$ ○ 0.99 mM $CuSO_4$

case. The nature of the problem is more clearly understood when one examines the data corresponding to τ = 50 ms, at which time both signal intensities should be negative, whereas they are, in fact, positive. As a second example, given that the null point of the 4.96 mM $CuSO_4$ solution is close to τ = 100 ms, all signals observed after that τ-time should be positive. In practice the value at τ = 150 ms is

negative and remains so until τ = 250 ms at which time it becomes positive. Conversely, the signal intensity of the 0.99 mM solution should be negative prior to its null point at τ = 400 ms, and thereafter become positive. Instead, the signal is positive from τ = 50-150 ms, negative between 250-400 ms, after which time it becomes positive again. Obviously, these fluctuations in signal sign made any attempt at quantitative measurements very difficult, since the absolute sign of the signal in a particular image was in serious doubt.

However, this phenomenon can be explained[41] and compensated for. The centre view of a 2D image has effectively no phase encoding gradient. The instrument software carries out a peak search on this view to set the attenuation based on the magnitude of the maximum intensity peak. A global phase correction is then carried out by making this maximum peak real and positive. All other signal signs are then relative to this peak. If it happens to be a negative-going peak then it is phase-corrected 180^{o} to become the maximum positive peak. Even when the attenuation is manually set, this phase correction is still carried out, resulting in the same signal-sign fluctuations. Thus, when τ = 50 ms, the signals from both the 0.99 mM and 4.96 mM solutions are negative, with the maximum intensity signal coming from the 0.99 mM solution. This automatically acts as the reference peak and is inverted 180^{o}. Since the

signal from the 4.96 mM solution is of the same sign, it too becomes positive. As another example, consider the image obtained when τ = 150 ms. At this τ-value the signal from the 0.99 mM solution should be negative, and that from the 4.96 mM solution positive; in practice the reverse is observed. This is due to the fact that the magnitude of the signal from the 0.99 mM solution is still larger than that from the 4.96 mM solution, by virtue of its longer T_1, and hence it again acts as the reference peak.

In order to get around the problem of fluctuating signal signs, the solutions under study were surrounded by a fast relaxing water bath (~10 mM $CuSO_4$ solution). This bath provided the most signal and was always positive for the range of τ-values being used. It therefore always acted as the reference peak and consequently ensured the correct phasing of all other signals. One unfortunate result of this, however, was that it was no longer possible to use the single projections from back projection images for measuring T_1, since they were too complex. Instead IR images were obtained, the intensities for each concentration of paramagnetic species measured from them directly, and subsequently processed.

In most cases, images obtained <u>in vivo</u> will not be affected by this method of phasing. However, if a region of long T_1 has a large volume, such as a fluid-filled cyst, then the negative signal which should be observed from this

region on an inversion-recovery image is, in fact, positive. The reason for this is the signal is phase corrected 180° to become the maximum positive peak. The result of this, of course, is that the signals from the surrounding regions are also inverted and have the wrong sign. It is clearly a problem which the manufacturer will have to deal with.

One method of phasing employed by other companies is to use a paired saturation-recovery image as a reference. Although this method removes the possibility of intensity ambiguities, it does have the disadvantage of having a longer total imaging time.

A further instrumental aberration was observed and is shown in the τ = 200 ms IR-image in Figure 25a, which consists of light and dark bands across the entire phantoms. The measurement was repeated on a large number of occasions over a period of months with identical results, ruling out the possibility of a transient instrumental problem.

At this τ-value, the signal from the 4.96 mM sample should be positive and that from the 0.99 mM negative. That these two signals have approximately equal magnitudes is shown in the image in Figure 25b as absolute intensities following magnitude reconstruction.

The banding can be explained[41] as follows: when the instrument carries out its peak search on the centre view of the 2D image, it is unable to find a maximum peak. The instrument effectively sees no signal due to the intensities

having equal but opposite sign. This results in a shift in the echo position, that is, there is a time shift of the time domain signal. This can be represented in the

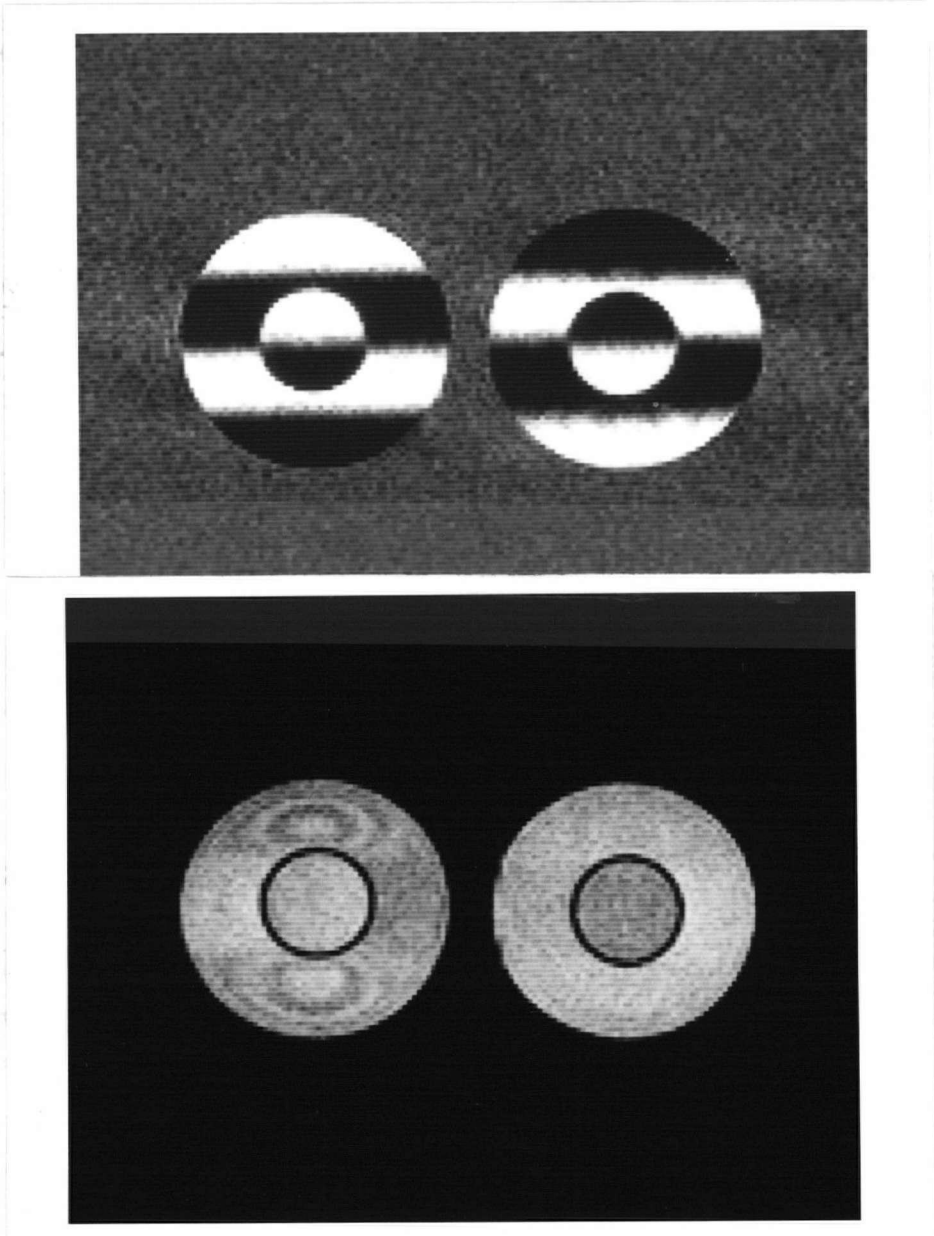

Figure 25: a. Inversion-recovery image of phantom used to demonstrate intensity ambiguities at τ = 200 ms.

b. The same image in a. after magnitude reconstruction.

following way: if f(t) has the Fourier transform F(ω), then the function f(t-a) has the transform $F(\omega)e^{-i\omega a}$ [42]. The derivation of this is straightforward:

$$f(t-a)e^{-i\omega t}dt = \int f(t-a)e^{-i\omega(t-a)}e^{-i\omega a}d(t-a) = e^{-i\omega a}F(\omega) \qquad (14)$$

In other words, if the time domain signal is shifted in time, its Fourier transform remains identical except that it gets multiplied by a phase factor which varies linearly with the frequency, ω, and is proportional to the time shift, a. This results in the phase shifts observed in the image in Figure 25a.

Additional proof that the banding observed is due to a time shift of the time domain signal was provided by the following experiment. As indicated previously, the actual IR pulse sequence used on this instrument has an additional 180° pulse which is applied at time t after the 90° pulse and subsequent data acquisition of the echo at 2t. In order to collect the echo at this time, the correct gradient sequence must be used. If t = 13 ms, then the read and phase encoding gradients required for the data acquisition are identical to those used for a spin-echo sequence with 2τ = 26 ms. If the time of data acquisition is left unchanged, and the above gradients substituted with those required for a spin-echo sequence that has 2τ = 20 ms, the result is a shift of the echo position in the time domain signal. This substitution gave rise to banded images like that shown in

Figure 25a. It is clear from these studies that any factor which causes a shift in time of the time domain signal, will give rise to the phase shifts observed on these images.

It was also possible to correct for these phase shifts using the fast relaxing background water bath, since there was no longer any possibility of the instrument misinterpreting the signals from the solutions being studied. This allowed useful data to be obtained for the range of τ-values required to determine T_1.

CHAPTER 2

QUANTITATION OF NMR PARAMETERS

The appearance of an NMR image is dependent on more than one parameter. Pulse sequences are chosen to provide images whose intensities are weighted towards one parameter, and which also provide the necessary differences in intensity between normal and diseased tissue for identification of pathology. The contrast provided by T_1 and T_2-weighted images are the most important. The optimum choice of pulse sequence is the one which provides the most tissue discrimination; this in turn depends on the relative T_1 and T_2-values. This chapter describes the measurement of T_1 and T_2 using the Picker International whole body imaging instrument. Both time constants are defined and the methods of measurement are described. The effects of imaging conditions and instrument limitations on the values of T_1 and T_2 obtained are examined.

a. Spin-Lattice Relaxation (T_1)

(i) Definition

The spin-lattice relaxation time (T_1) can be defined as the time constant of the process whereby an ensemble of nuclear spins return to thermal equilibrium with their lattice after perturbation. This form of relaxation involves an exchange of energy between the spin and the lattice and occurs due to interaction between the

fluctuating field generated by the precessing nuclei and those generated in the lattice by movement of other magnetic nuclei. These interactions can involve a number of different processes[43], namely:

1. magnetic dipole-dipole interactions
2. electric quadrupole interactions
3. chemical shift anisotropy interactions
4. scalar-coupling interactions
5. spin rotation interactions.

Any mechanism which gives rise to fluctuating magnetic fields at a nucleus is a possible relaxation mechanism. All aqueous solutions studied in this section contained paramagnetic species. Since the magnetic moments of the unpaired electrons in these paramagnetic species are ca. 10^3 times greater[44] than the nuclear magnetic moments of the water protons, they give rise to much larger local fields, and hence dominate the relaxation of the water.

In a dilute solution of a paramagnetic species, the relaxation of the solvent nuclei (in this case water) will be dominated by the effects of the unpaired electrons on the solvation sphere of the metal ion[45]. The bound water molecules and the bulk solvent have different relaxation times. Rapid exchange of the water molecules and the protons of the molecules within the two phases gives rise to a single observed relaxation time.

If the random fluctuating magnetic fields at the site

of the paramagnetic species occur at the Larmor frequency of the solvent protons then T_1 relaxation can occur, i.e. it induces a nuclear spin transition from $I_z = -1/2$ to $+1/2$.

The T_1 of a nucleus bound to a paramagnetic site is given by the following equation[45]:

$$\frac{1}{T_1} = \frac{2}{15} \frac{\gamma_I^2 g^2 S(S+1)\beta^2}{r^6} \left(\frac{3\tau_c}{1+\omega_I^2\tau_c^2} + \frac{7\tau_c}{1+\omega_S^2\tau_c^2} \right) \qquad (15)$$

$$+ \frac{2}{3} S(S+1)\left(\frac{A}{\hbar}\right)^2 \left(\frac{\tau_e}{1+\omega_s^2\tau_e^2} \right)$$

The first terms arise from the dipole-dipole interaction between the electron-spin, S, and the nuclear spin, I, which is characterized by the correlation time, τ_c. The second terms arise from modulation of the scalar interaction (often called isotropic nuclear-electron spin-exchange interaction) which is characterized by correlation time, τ_e. The electronic and nuclear Larmor precession frequencies are given by ω_S and ω_I, γ_I is the gyromagnetic ratio, β is the Bohr magneton, S is the total electron spin, r is the distance between the nucleus and the paramagnetic ion, and $A/\hbar$ is the electron-nucleus hyperfine coupling constant in Hz. The correlation times are defined as follows:

$$\frac{1}{\tau_c} = \frac{1}{\tau_s} + \frac{1}{\tau_M} + \frac{1}{\tau_R} \qquad (16)$$

$$\frac{1}{\tau_e} = \frac{1}{\tau_s} + \frac{1}{\tau_M} \qquad (17)$$

where τ_M = life-time of a nucleus in the bound site

τ_R = rotational correlation time of the bound paramagnetic ion

τ_s = electron-spin relaxation time.

(ii) Measurement of T_1

The utilization of T_1 in NMR spectroscopy, including methods of measurement, is well documented[46-50]. In this study, the method known as inversion-recovery was used to carry out the measurements on the aqueous solutions, and is described below.

The pulse sequence used in the inversion-recovery method is given below:

$$(-180°-\tau-90°-\text{Data acquisition}-)_n \qquad (12)$$

The intensity at a particular τ-value is given by equation 7,

$$I_{(\tau)} = I_o(1-2\exp(-\tau/T_1)) \qquad (7)$$

which is obtained by integration of the Bloch equation describing decay of M_z,

$$\frac{dM_z}{dt} = -(M_z-M_o)/T_1 \qquad (18)$$

where M_o = thermal equilibrium value of M_z.

The intensity is measured over a range of τ-values, then T_1 may be obtained from an exponential fit of the data or a semi-log plot. The repetition time must be sufficiently long ($5T_1$) to allow the nuclei to return to their equilibrium state before reapplication of the 180° pulse.

In the imaging experiment the z-component of the observable magnetization may not be fully inverted due to the radiofrequency field inhomogeneity over the large volumes being studied. Incomplete inversion of the magnetization can be corrected for in the data processing by fitting the data to equation 13, which includes a correction factor, W, for the 180° pulse[40],

$$I_{\tau} = I_0\{1-[1+W(1-\exp(-k/T_1)]\exp(-\tau/T_1)\} \qquad (13)$$

where I_0 = intensity at $\tau >> T_1$

k = waiting period between data acquisition and reapplication of 180° pulse

W = correction factor for 180° pulse.

A phantom consisting of 2 cm diameter vials placed in a large petri dish was constructed as shown in Figure 20 (p.31). The vials were filled with accurately known concentrations of $CuSO_4$ and manganese(II) chloride ($MnCl_2$) solutions, and T_1 measurements were carried out using the inversion-recovery method.

Copper(II) Sulphate Solutions

Inversion-recovery horizontal (xz) slice images were obtained with τ-values in the range 50-1000 ms and a TR of 4 sec plus τ. The mean intensities over 2.6 cm^2 at the centre of the vials were obtained directly from the images using the cursor on the instrument and a three-parameter exponential fit was carried out on the data using equation 13.

Manganese(II) Chloride Solutions

Inversion-recovery images were obtained as before with τ-values in the range 10-1000 ms and TR of 3 sec plus τ. The intensities were obtained once again from the centres of the vials, and processed in the same way as the $CuSO_4$ data.

A 95% accuracy linear regression analysis was carried out on all results, and the T_1 values, plus or minus two standard deviations, are given in Table II.

Table II: T_1 values for various concentrations of $CuSO_4$ and $MnCl_2$ solutions obtained at 20 (± 1)°C using the inversion-recovery method. Two values are given for each concentration corresponding to two different positions in the receiver coil.

Solution	Concentration (mM)	T_1 (ms)
$CuSO_4$	4.96	108 ± 10
	4.96	126 ± 4
	2.54	245 ± 6
	2.54	243 ± 13
	0.99	519 ± 4
	0.99	548 ± 2
$MnCl_2$	0.67	103 ± 1
	0.67	106 ± 1
	0.34	189 ± 2
	0.34	188 ± 1
	0.16	350 ± 8
	0.16	340 ± 8
	0.06	659 ± 9
	0.06	663 ± 8

(iii) Computed T_1

The software of the instrument, developed by Picker International, has the capability of carrying out T_1 computations.

Two images are required to carry out these T_1 computations: an inversion-recovery and a spin-echo image. The repeat times must be equal in both images. The intensities for each image are given in equations 19 and 20.

$$I_{IR} = I_o \exp(-2t/T_2)[1-(2-2\exp(-k/T_1) + \exp((-k-\tau)/T_1)]\exp(-t/T_1) \quad (19)$$

$$I_{SE} = I_o \exp(-2\tau/T_2)[1-2\exp(-k/T_1) + \exp(-TR/T_1)] \quad (20)$$

$$S_o = \frac{I_{IR}}{I_{SE}} = \frac{1-(2-2\exp(-k/T_1) + \exp(-\tau-k/T_1)\exp(-t/T_1)}{(1-2\exp(-k/T_1) + \exp(-TR/T_1)} \quad (21)$$

The ratio of these intensities is given in equation 21. Taking the ratio eliminates the image intensity dependence on the equilibrium magnetization and T_2, then T_1 may be obtained from a look-up table, which is a plot of S_o versus T_1. T_1 computations were carried out on solutions containing the same paramagnetic ion concentration as in (ii) and the numbers compared. The results are given in Table III. The computed T_2 values are given as the mean value from 2.6 cm^2 at the centre of the vials.

Table III: Computed T_1 values for various concentrations of $CuSO_4$ and $MnCl_2$ solutions obtained at 20 (± 1)°C. Two values are given for each concentration, corresponding to two different positions in the receiver coil.

Solution	Concentration (mM)	Computed T_1 (ms)
$CuSO_4$	4.96	117
	4.96	123
	2.54	245
	2.54	235
	0.99	556
	0.99	548
$MnCl_2$	0.67	83
	0.67	98
	0.34	192
	0.34	188
	0.16	357
	0.16	350
	0.06	678
	0.06	679

(iv) Effects of a Spin-echo Readout

After application of the 90^{o} RF pulse in an IR sequence, not all the nuclear spins will precess at the same Larmor frequency; they will be out of phase. This is due to the presence of the field gradient. Unless the spins are in phase, the xy magnetization is not detected. In order to get around this, a second 180^{o} refocusing pulse is applied after a short time (13 ms) and the spin-echo collected 2τ (26 ms) after the 90^{o} pulse. This is referred to as a spin-echo readout. During the time 2τ, spin-spin relaxation can occur, which may introduce a further source of error in the measurement of T_1, since the equation for the intensity at any τ-value will have not only the exponential T_1 term but also an exponential T_2 term. The method of data processing used in (ii) does not take into account the fact that a SE readout is employed. In theory, it should be possible to treat the exponential T_2 term as a constant, since it is identical in every sequence. In order to check this, two different spin-echo readouts were used and the T_1 values compared. Spin-echo τ-values of 13 ms and 20 ms were employed. The data for τ = 13 ms is given in Table II. The use of a SE readout will have more of an effect on short T_2 values; therefore this experiment was only carried out on the $MnCl_2$ solutions, where T_2 is considerably shorter than T_1. The results for a τ-value of 20 ms are shown in Table

IV, together with the computed T_1 values using the same readout.

Table IV: T_1 values for various concentrations of $MnCl_2$ solution, obtained at 20 (± 1)°C using the inversion-recovery method, and a spin-echo readout with τ = 20 ms. Computed T_1 values with the same readout are given for comparison. Two values are given for each concentration, corresponding to two different positions in the receiver coil.

Solution	Concentration (mM)	T_1 (ms)	Computed T_1 (ms)
$MnCl_2$	0.67	100 ± 3	78
	0.67	107 ± 10	73
	0.34	191 ± 7	190
	0.34	189 ± 5	189
	0.16	343 ± 3	346
	0.16	335 ± 3	352

(v) Effects of Proton Density

The signal intensity observed on an NMR image is dependent not only on the relaxation times of the protons but also on the number of protons giving rise to the signal. This is referred to as the proton density. A number of slice thicknesses are available for use on the imaging

instrument. Varying the slice thickness may introduce a further source of error in the measurement of T_1, since it changes the proton density contribution to the observed signal.

If, for a series of IR images, the same slice thickness is applied for each image, it should be possible to treat the proton density factor as a constant. This was tested by using two additional slice thicknesses of 5 mm and 20 mm and running inversion-recovery T_1 experiments on the $MnCl_2$ solutions. The images were processed as before and the results are shown in Tables Va and Vb, together with computed T_1 values with the same slice thickness.

Table Va: T_1 values for various concentrations of $MnCl_2$ solution, obtained at 20 (± 1)°C using the inversion-recovery method, and a slice thickness of 20 mm. Computed T_1 values are given for comparison.

Solution	Concentration (mM)	T_1 (ms)	Computed T_1 (ms)
$MnCl_2$	0.34	198 ± 2	174
	0.34	182 ± 5	178
	0.16	330 ± 11	349
	0.16	350 ± 6	338
	0.06	630 ± 13	682
	0.06	689 ± 22	675

Table Vb: T_1 values for various concentrations of $MnCl_2$ solution, obtained at 20 (± 1)°C using the inversion-recovery method, and a slice thickness of 5 mm. Computed T_1 values are given for comparison.

Solution	Concentration (mM)	T_1 (ms)	Computed T_1 (ms)
$MnCl_2$	0.34	183 ± 4	187
	0.34	186 ± 3	184
	0.16	349 ± 2	333
	0.16	346 ± 1	337
	0.06	662 ± 12	650
	0.06	696 ± 4	683

(vi) Multiexponential Relaxation Behaviour

Multiexponential relaxation behaviour may be observed for an isotropic solution containing protons with different physical characteristics, such as a mixture of oil and water, if proton exchange does not occur or is slow on the NMR time scale. In an imaging measurement, additional sources give rise to multiexponential relaxation behaviour; of these, volume averaging is the most significant. An image can be obtained by selectively exciting a slice 10 mm thick. Within this thickness there may be water protons in different compartments or in different types of tissue,

which are not exchanging. The signal contribution from each proton source depends on its volume and on the pulse sequence used to excite the slice. The resulting image intensity in each pixel is the sum of the signal contributions through the slice. For proton NMR imaging studies of mammalian tissues, the signals of water and fat will overlap due to the negligible chemical shift difference between the two signals at the low magnetic field used to obtain the images. This could also give rise to multiexponential relaxation behaviour, since the mobile fat protons may have a different T_1 and T_2 than those of water.

If more than one exponential decay is present, the signal intensity observed for a particular τ-value is given by equation 22.

$$I_{(\tau)} = \sum_{i=1}^{n} I_{oi}(1-2\exp(-\tau/T_{1i})) \qquad (22)$$

where n = number of exponentials required for an adequate description of the data, taking into account experimental accuracy, σ_i.

Computer programs are available for analysis of relaxation data. These programs fit a chosen number of exponentials to the data, and thus provide the different relaxation times contributing to the signal.

Consider two compartments, between which there is no exchange, and having T_1 values of 245 ms and 519 ms. If they are excited simultaneously in the same slice, then the

observed signal intensity for a given τ-value in an inversion-recovery image is given by the sum of the intensities for each compartment. The resultant magnetization plot, together with the individual plots for each compartment, are given in Figure 26, and the observed T_1 is 338 ms. This means that the computed T_1 images can

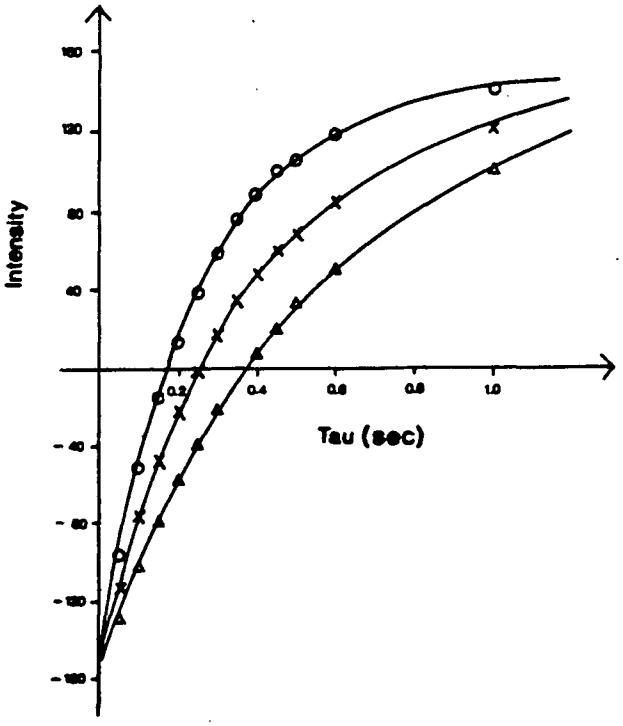

Figure 26: Plot of intensity versus tau demonstrating multiexponential relaxation behaviour.

○ 2.54 mM $CuSO_4$ △ 0.99 mM $CuSO_4$

✕ 2.54 mM $CuSO_4$ + 0.99 $CuSO_4$

only provide observed T_1-values, giving no indication as to their source. In order to determine whether the observed T_1 is the result of multiexponential relaxation behaviour, the intensity must be measured as a function of τ.

(vii) Discussion

The T_1 data are summarized in Figure 27. The results show that useful T_1 measurements can be made in the range 100-600 ms. Although this is not a large range, it does encompass the T_1-values of many tissues, and in particular those of the grey and white matter of the brain. Comparison

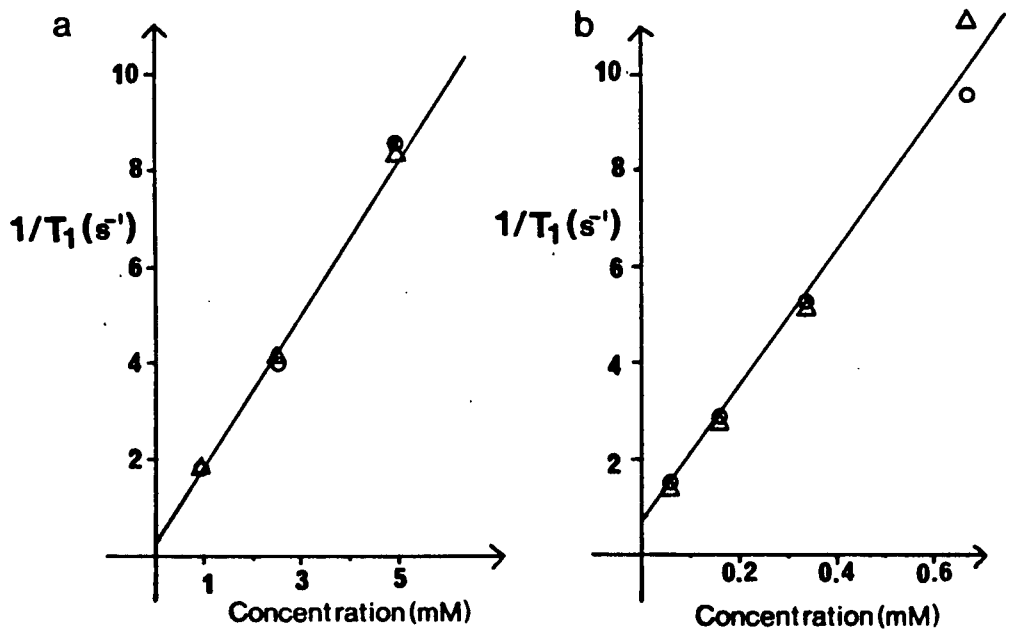

Figure 27: a. Plot of spin-lattice relaxation rate versus concentration for $CuSO_4$ solutions.

o IR data

Δ Computed data

b. Plot of spin-lattice relaxation rate versus concentration for $MnCl_2$ solutions.

o IR data

Δ Computed data

of the T_1 data obtained using the inversion-recovery method with that from the computed images gives a correlation within 10%. The values obtained from the computed images are therefore useful, since they can be obtained more rapidly than the inversion-recovery data. However, it is not possible to make error estimates on these numbers, or to extract information on multiexponential relaxation behaviour.

Taking into account the random error in the data together with the effects of inhomogeneity across the coil, reproducible values of T_1 can be obtained ± 12%. In most cases the errors were somewhat less than this. The same trend was observed for data obtained using a longer spin-echo read time and again when the slice thickness was varied. Comparison of the mean values and errors obtained for data under different imaging conditions shows a correlation of less than 5% between the results. The data demonstrates that over the T_1 range studied, it is possible to treat many conditions of the imaging experiment as constants without affecting the measured T_1-values. The T_1 values are within 12% of literature values measured under conventional spectroscopic conditions, with no magnetic field gradients present[51].

These findings contradict those reported in the literature by Rosen, Pykett and Brady[52], who state that corrections must be made to T_1 data for the effects of slice

selection and a spin-echo readout.

Multiexponential relaxation behaviour arising from volume averaging is a problem in imaging. It is important to be aware of it when applying NMR imaging *in vivo*. The observed T_1-values may arise from more than one tissue type; however, the values can be compared if the same slice is excited in serial studies. This is considered again in Chapter 3.

b. Spin-spin Relaxation (T_2)

(i) Definition

Immediately after a spin system has been perturbed by a 90^{o} pulse, for example, the spins of the individual nuclei are in phase. They then begin to exchange energy with one another leading to the decay of the magnetization in the x'y' plane, $M_{y'}$, with a time constant T_2. In addition, inhomogeneities in the static magnetic field, ΔB_o, will result in a range of Larmor precession frequencies which also cause $M_{y'}$ to decay. Overall $M_{y'}$ decreases to zero with a time constant T_2^* which includes a term for the field inhomogeneity (equation 23).

$$\frac{1}{T_2^*} = \frac{1}{T_2} + \frac{\gamma \Delta B_o}{2} \qquad (23)$$

Fluctuating fields in the x, y and z directions all have an effect on T_2.

The T_2 of a nucleus bound to a paramagnetic site is given by the following equation 24.[45]

$$\frac{1}{T_2} = \frac{1}{15}\frac{\gamma_I^2 g^2 S(S+1)\beta^2}{r^6}\left[4\tau_c + \frac{3\tau_c}{1+\omega_I^2\tau_c^2} + \frac{13\tau_c}{1+\omega_S^2\tau_c^2}\right] \qquad (24)$$

$$+ \frac{1}{3}S(S+1)\left(\frac{A}{h}\right)^2\left[\frac{\tau_e}{1+\omega_s^2\tau_e^2} + \tau_e\right]$$

The parameters are the equivalent of those in the T_1 equation (p.47) and the terms arise from the same types of interactions as those described for T_1.

(ii) Measurement of T_2

As previously mentioned, the magnetization decay is dependent not only on T_2, but on the static magnetic field inhomogeneity. It is therefore not possible to use T_2^* as a measure of T_2.

In 1950, Hahn[27] proposed the use of the spin-echo method to overcome the dephasing effect of the field inhomogeneity. The principle behind the spin-echo technique was shown in Figure 6, page 13. Immediately after application of the 90° pulse, all the nuclear spins are in phase, i.e. they are all precessing with the same Larmor frequency. The presence of any inhomogeneity in the static magnetic field means that not all nuclei will be experiencing the same external field, and the result of this is dephasing of the spins. If the spins are allowed to dephase for a time τ, followed by application of a 180° pulse about the x-axis, they will refocus or come back into

phase at time 2τ, when they can be detected. The intensity is measured as a function of 2τ, thus providing a value of T_2 by carrying out either a logarithmic plot or an exponential fit. The repeat time for the sequence must be sufficiently long to allow return to equilibrium between successive pulses, just as in the IR T_1 experiment. The use of the spin-echo method is limited however, since molecular diffusion may occur during the refocusing of the magnetization resulting in a reduction in the echo amplitude. Carr and Purcell[28] have shown that the effect of diffusion on a spin-echo experiment is dependent on the spatial magnetic field gradients (G), the diffusion coefficient (D) and the time during which diffusion can occur. It is given by equation 10.

$$I_{(2\tau)} = I_o \exp(-2\tau/T_2) \exp\left(-\frac{2}{3}\gamma^2 G^2 D\tau^3\right) \qquad (10)$$

The τ^3 dependence means that the effects of diffusion will be much more pronounced for large values of T_2. The effects of diffusion can be overcome, to a great extent, by using the Carr-Purcell method[29], which is a modification of the Hahn spin-echo method. The Carr-Purcell pulse sequence is given in equation 25,

$$(90°-\tau-180°-\tau-[\text{echo}]-\tau-180°-\tau-[\text{echo}]-.....) \qquad (25)$$

Positive and negative echoes are alternately formed. This method has two advantages: it saves time and by making τ

short the effects of diffusion may be virtually eliminated. One drawback is that pulse imperfections may cause incomplete rephasing of the spins resulting in error. This sequence is not available on the instrument used for these studies.

The same phantom constructed for the T_1 measurements was also used for the T_2 measurements. Horizontal (xz) SE slice images were obtained, with τ-values in the range 13-160 ms and TR of 3 sec plus τ, for the $CuSO_4$ and $MnCl_2$ solutions. The intensities were again obtained directly from the images and an exponential fit to equation 9 was carried out to determine T_2,

$$I_{(2\tau)} = I_o \exp(-2\tau/T_2) \qquad (9)$$

where I_o = equilibrium magnetization.

A 95% accuracy linear regression analysis was carried out on all T_2 values obtained, and values plus or minus two standard deviations are given in Table VI.

Table VI: T_2 values for various concentrations of $CuSO_4$ and $MnCl_2$ solution, obtained at 20 (± 1)^{o}C using the spin-echo method. Two values are given for each concentration corresponding to two different positions in the receiver coil.

Solution	Concentration (mM)	T_2 (ms)
$CuSO_4$	4.96	116 ± 4
	4.96	116 ± 4
	2.54	194 ± 10
	2.54	191 ± 15
	0.99	313 ± 22
	0.99	354 ± 26
$MnCl_2$	0.67	46 ± 2
	0.67	46 ± 3
	0.34	78 ± 3
	0.34	78 ± 5
	0.16	136 ± 7
	0.16	136 ± 4
	0.06	244 ± 14
	0.06	248 ± 9

(iii) Computed T_2

Two spin-echo images are required to carry out a T_2 computation using the Picker International instrument software. These images must have equal repeat times and different echo times.

The ratio of these intensities is then taken, thus eliminating the image intensity dependence on the equilibrium magnetization and T_1. T_2 is then obtained from a look-up table, just as for T_1. The ratio is given in equation 26. T_2 computations were carried out on the same solutions as in (ii), using spin-echo τ-times of 20 ms and 40 ms, and the results are given in Table VII.

$$S = \frac{I_{SE_1}}{I_{SE_2}} = \frac{(1-2\exp(-k_1/T_1) + \exp(-TR/T_1)\exp(2\tau_1/T_2)}{(1-2\exp(-k_2/T_1) + \exp(-TR/T_1)\exp(2\tau_2/T_2)} \qquad (26)$$

Table VII: Computed T_2 values for various concentrations of $CuSO_4$ and $MnCl_2$ solutions, obtained at 20 ($\pm$ 1)^{o}C. Two values are given for each concentration corresponding to two different positions in the receiver coil.

Solution	Concentration (mM)	T_2 (ms)
$CuSO_4$	4.96	120
	4.96	131
	2.54	219
	2.54	221
	0.99	522
	0.99	548
$MnCl_2$	0.67	43
	0.67	44
	0.34	77
	0.34	78
	0.16	135
	0.16	137
	0.06	414
	0.06	443

The effect of varying the combination of τ-time on the resultant T_2 values was also examined. Computed T_2 measurements were carried out on the $MnCl_2$ solutions, using different τ-times, and the results are given in Table VIII.

Table VIII: Computed T_2 values for various concentrations of $MnCl_2$ solutions, obtained at 20 (± 1)°C using various combinations of τ-times. Two values are given for each concentration corresponding to two different positions in the receiver coil.

Concentration (mM)	τ-times (ms)		
	20,40	20,60	40,60
0.67	43	43	44
0.67	44	43	46
0.34	77	77	71
0.34	78	71	69
0.16	135	124	123
0.16	137	129	122

(iv) Effects of Diffusion

Only the SE method is available for measuring T_2 using the whole body imaging instrument.

As expected, when attempts were made to measure long T_2 values, the effects of diffusion resulted in abnormally

low values of T_2. A maximum value of 200 ms could be measured. The effects of diffusion on the computed T_2 values are minimized because a ratio is taken and, as a result, above T_2 = 200 ms the computed values are higher than those obtained using the exponential fits to the SE data.

(v) Discussion

The T_2 data is summarized in Figure 28. For T_2 values in the range 40-200 ms, the difference between spin-echo data and the computed T_2 values is 15% or less. The computed T_2 images are useful, since not only can they provide a quick indication of the T_2-value but they also minimize the effects of diffusion, thereby allowing the study of longer T_2. However, just as for the computed T_1 values, it is not possible to make error estimates or to extract information on multiexponential relaxation behaviour from these numbers.

Above the range of 40-200 ms, the effects of diffusion increase, as one would expect. The T_1/T_2 ratio for water doped with $CuSO_4$ is close to unity, and once the T_2 value gets above 200 ms, the spin-echo data does not reflect this.

Comparison of literature values[51] obtained at the same field using the Carr-Purcell method, as modified by Meiboom and Gill[53], shows a correlation of a few percent for the range 40-200 ms.

Although this is a narrow range, many tissue T_2-values lie within it, in particular those of brain tissue.

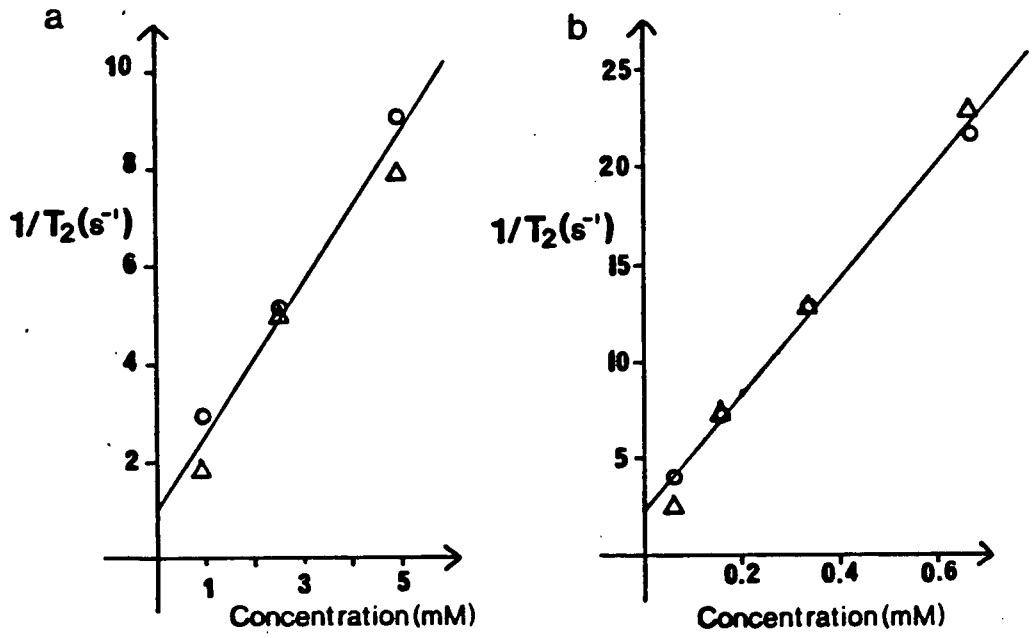

Figure 28: a. Plot of spin-spin rate versus concentration for $CuSO_4$ solutions.

o SE data

Δ Computed data

b. Plot of spin-spin relaxation rate versus concentration for $MnCl_2$ solutions

o SE data

Δ Computed data

CHAPTER 3

Applications of Quantitative NMR Imaging

This chapter describes in detail an experimental application of quantitative NMR imaging *in vivo*. The reader is introduced to the structure of the brain and spinal cord, and the diseases of interest in this study. How these diseases affect the central nervous system is also explained.

(i) Background

The nerve cells, or neurons of the brain and spinal cord consist of cell bodies and axons, as shown in Figure 29. It is along the axon that the nerve impulses travel, and the axons of different neurons communicate with one

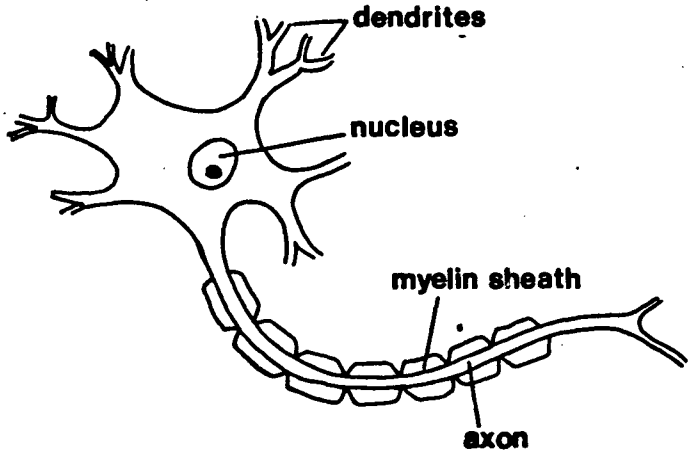

Figure 29: Diagram of nerve cell.

another at junctions known as synapses. Many axons are surrounded by a myelin sheath, which increases the rate at

which the axon can conduct impulses. The myelin allows what is known as saltatory conduction. This is where conduction is by a mixture of cable properties of the nerve fibres, as well as by chemical mechanisms.

In demyelinating diseases, such as Multiple Sclerosis (MS), this myelin sheath is broken down, resulting in a decrease in the speed at which a nerve impulse can travel along the axon. The areas of abnormality in MS are large (> 3 mm), and of more than one type. They can occur anywhere in the central nervous system, predominantly in the white matter but also in the grey matter.

One of the major problems in mapping the course of MS is that the only data available on humans is post mortem, by which time the disease is usually in the chronic stage. This means that little is known about the pathology of the early stages of the disease. For this reason, animal models for MS have been developed in order to study the mechanism of the development of the early lesion. One such model is Experimental Allergic Encephalomyelitis (EAE).

NMR imaging has provided an opportunity for serially studying both MS and EAE with no known risk to the subject. The ability to detect abnormal areas is a result of changes in the NMR characteristics of the protons. The molecular environment of the protons changes, which in turn affects their NMR properties. It is these molecular changes that must eventually be charted, since they are responsible for

the changes observed as gross pathology and on the NMR images. This was the basis for undertaking these studies of EAE in primates.

It is known that the first event in EAE is inflammation leading to haemorrhagic necrosis. Eventually demyelination is also present. In this project serial studies have shown that the progression of EAE can be followed using NMR imaging. Furthermore, measurement of T_1 and T_2 as a function of time provides an indication of change on a molecular level *in vivo*.

(ii) Induction of EAE and NMR Imaging Protocol

EAE was induced in a male *Macaca fascicularis* monkey, weighing 3 kg, by injection of 0.15 mL of a water-in-oil emulsion containing 15 mg monkey myelin basic protein and 0.5 mg heat killed *Mycobacterium tuberculosis* intradermally in the hindfoot pads[54]. The animal was obtained from the Bureau of Biologics Breeding Colony in Ottawa and was housed first in the UBC Animal Care Facility on South Campus Road, then after induction of the disease, he was moved to the Acute Care Unit animal care facility.

NMR imaging data were collected on the Picker International whole body imaging system using a receiver coil with an aperture of 15 cm. Data were collected using multi-slice spin-echo and inversion-recovery pulse sequences, both of which provided 8 contiguous 5 mm thick

slices. Echo delays (2τ) of 40 ms and 60 ms were employed in the spin-echo sequences. A τ-time of 400 ms was used for the inversion-recovery sequence, and in all sequences the repeat time was 2 sec. These parameters were chosen in order to allow direct comparison with human MS data, and the choice of pulse sequences would allow computation of T_1 and T_2.

As indicated in Chapter 2, volume averaging can give rise to multiexponential relaxation behaviour. When images are obtained from the monkey's brain, both grey and white matter may be excited in the same slice. If the results of serial scanning were to be comparable, then accurate repositioning of the monkey's head was essential; the same slices had to be excited in each set of images obtained. This was achieved in the following way: using Polyflex-II, a commercially available thermoplastic polymer used in the PET program, a mould was made of the monkey's head, and fitted to the receiver coil. This allowed repositioning within 2 mm for each set of scans. Figure 30 shows the position of the monkey in the scanner and the slice images being obtained.

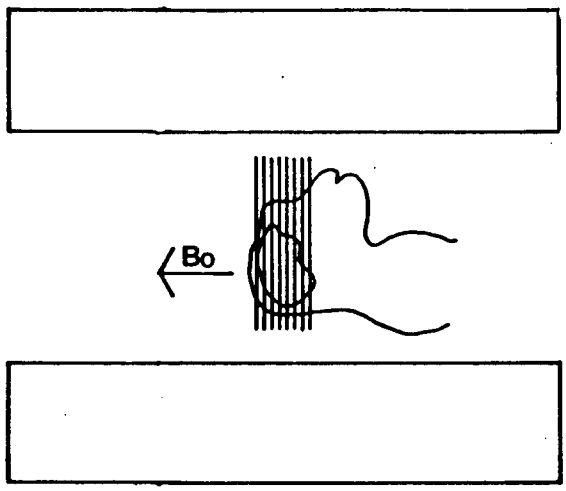

Figure 30: Diagram showing the position of the monkey in the instrument and the slices being obtained.

(iii) Development of EAE Using NMR Imaging

The monkey was anaesthetized for imaging using 0.8 mL combination of ketamine and rompun, (12:1 ratio) the effects of which lasted 1.5-2 hours. He was checked three times every 24 hours for the onset of clinical signs[55] and scanned daily until the detection of the first abnormal area, after which time he was scanned approximately every 10 hours.

The monkey developed a definite abnormal area in the white matter of the left cerebral hemisphere, 16 days after inoculation and before the onset of any obvious clinical signs. The image obtained on that day is shown in Figure 31. A spin-echo pulse sequence with an echo-delay of 40 ms was used to obtain the image. The arrow indicates the abnormal area. After the 180^{o} refocusing pulse is applied

in the spin-echo sequence, the signal intensity observed from the abnormal area is greater than that from normal white matter due to an increase in T_2, a decrease in its relaxation rate. The abnormal area therefore appears brighter than normal tissue on a spin-echo image.

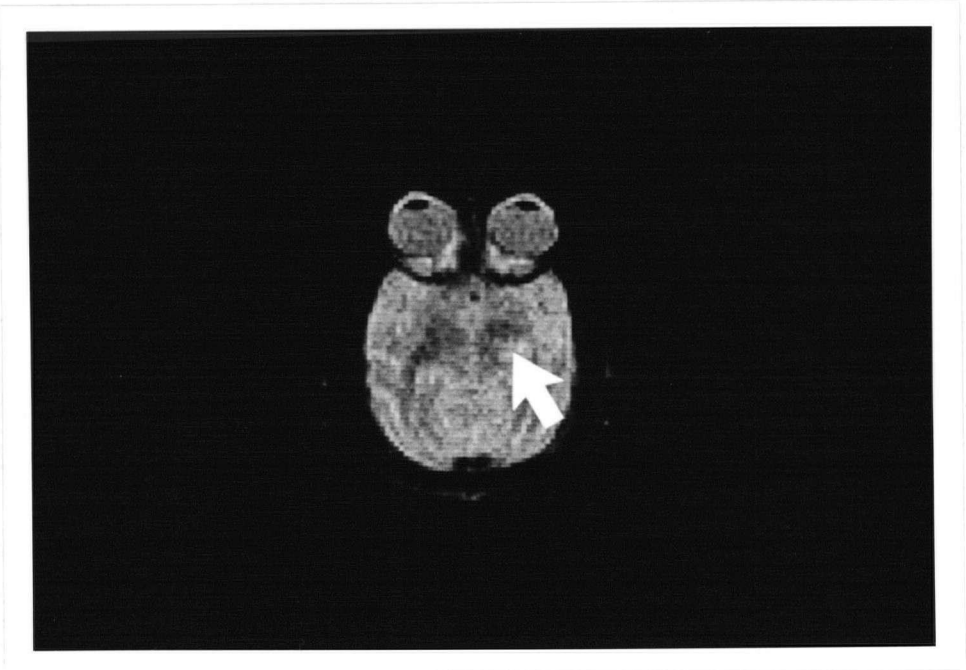

Figure 31: Transverse SE image of the monkey's brain, showing the abnormal area in the left hemisphere (right side of image).

The development of the disease could be easily followed. Figure 32 shows a series of spin-echo images obtained from the monkey. The number of days after inoculation are as indicated in the caption.

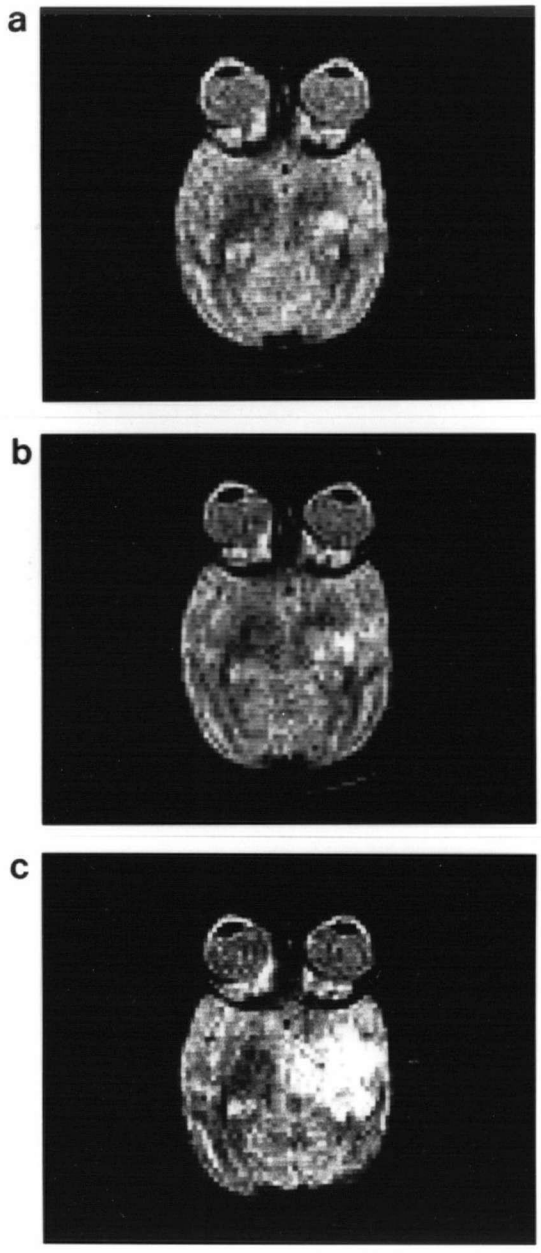

Figure 32: Series of three spin-echo images obtained from the monkey's brain.

a. 16.25 days after inoculation

b. 16.75 days after inoculation

c. 18.42 days after inoculation

The light areas are abnormal.

(iv) Quantitation of NMR Parameters

T_1 and T_2 computations were carried out on the abnormal areas from the day of appearance until death. Table IX and X contain sample series of these measurements, obtained from the same slice during serial scanning.

Table IX: T_1 values as a function of time after induction of EAE, for white matter (WM) and grey matter (GM) which appear normal, and the lesion.

Time (Days)	T_1 (ms)		
	WM	GM	Lesion
16.25	370	530	440
16.75	370	530	480
17.12	390	520	500
17.67	380	530	540
18.04	390	530	570
18.42	370	510	590
18.92	370	520	600

Table X: T_2 values as a function of time after induction of EAE, for white matter (WM) and grey matter (GM) which appear normal and the lesion.

Time (Days)	T_2 (ms)		
	WM	GM	Lesion
16.25	110	110	150
16.75	110	110	150
17.12	120	140	200
17.67	120	110	180
18.04	120	100	220
18.42	100	90	240
18.92	110	110	240

Table XI contains T_1 data for different slices, obtained from the monkey's brain immediately prior to death. These values, together with those for T_2, were correlated with the pathology found post mortem.

Table XI: T_1 values from five different slice images immediately prior to death for white matter (WM) and grey matter (GM) which appear normal, and the lesion.

Slice	T_1 (ms)		
	WM	GM	Lesion
1	390	490	610
2	390	450	600
3	390	470	650
4	390	470	560
5	400	500	660

(v) Discussion

These studies were based on the postulate that NMR imaging can be used to detect and follow the development of EAE in primates. Experimental results have shown this to be true[56].

EAE can be detected in primates before the onset of clinical signs using NMR imaging. This has implications for the study of MS in humans; some MS lesions appear unaccompanied by new clinical symptoms. It may be that the first lesion observed in the monkey, which was not reflected clinically, is pathologically similar to clinically asymptomatic MS lesions in humans.

Characterization of these asymptomatic lesions in MS

could provide the information necessary to understand and chart the progression of the disease. This is an exciting topic for further exploration.

The progress of EAE in primates can be easily followed using NMR imaging. The time of appearance of individual lesions could be noted, which allowed mapping of the disease post mortem. Until now, this information on the whole disease process has been unobtainable. Accurate repositioning is essential, since volume averaging could lead to discrepancies in the appearance of the image, and in quantitative measurements, if more than one tissue type is contributing to the signal observed from a particular slice.

Comparison of the relaxation data obtained immediately prior to death with the histopathology, reveals that longer T_1 and T_2 values are associated with the presence of inflammation, haemorrhagic necrosis and demyelination. In the initial stages of the disease, not all three types of pathology are present. The changes in T_1 and T_2 over time reflect the molecular changes occurring due to the progression of the disease. The individual changes in T_1 and T_2 from detection until death (60% and 140% respectively) are sizeable compared with the errors of 12% and 15% found in the studies on water doped with paramagnetic species, described in Chapter 2. This means that the initial lesion can be distinguished from those occurring later by these changes in T_1 and T_2. In other

words, it should be possible to distinguish between areas of inflammation (which is an early event) and areas containing demyelination (which occurs later in the progress of the disease.) In addition to this, there is an elevation in T_1 before the lesion is visible on the NMR image. If this elevation is reproducible, and is large in comparison to the errors involved, then this indicates that a fresh lesion can be detected by changes in T_1 before it is visible on the image.

The results of this work have shown that quantitative NMR imaging has the potential for answering many pertinent questions regarding EAE in primates and eventually MS in humans.

CONCLUSIONS

1. It has been shown that reproducible values of the spin-lattice relaxation time (T_1), in the range 100-600 ms, can be obtained using the inversion-recovery method, at a field strength of 0.15 Tesla on water doped with various concentrations of paramagnetic species. It has also been shown that changing the image slice select gradient and the spin-echo read time do not affect the resultant T_1 values. Using scatter in results observed under a range of conditions, it has been estimated that the uncertainty in the T_1 values obtained using the inversion-recovery method is less than 12%. This method produces T_1 values which are consistent with the results of the two-point computational method, and in addition, makes error estimates possible. The inversion-recovery method can also provide information on multiexponential relaxation behaviour, which is important for *in vivo* studies. The T_1 values obtained are within 12% of literature values measured under conventional spectroscopic conditions with no magnetic field gradients present.
2. Results show that reproducible values of the spin-spin relaxation time (T_2) in the range 40-200 ms, can be obtained using the spin-echo method, at a field strength of 0.15 Tesla on water doped with paramagnetic species. Above this range the effects of diffusion

become important, resulting in abnormally low values of T_2, compared with literature values obtained using the Carr-Purcell method, as modified by Meiboom and Gill. The errors estimated for T_2 in the range 40-200 ms are ± 15% and the results are within 12% of the literature values. The spin-echo method provides T_2 values in the range 40-200 ms, which are consistent with values obtained using the two-point computational method, and in addition makes error estimates possible. The computational method takes the ratio of two spin-echo images with different τ-values, which minimizes the effects of diffusion and provides realistic values for T_2 longer than 200 ms.

3. NMR imaging can detect Experimental Allergic Encephalomyelitis (EAE) in primates before the onset of clinical signs. The technique can be used to follow the development of the disease, which allows mapping of its pathological progression. The progression of the disease is accompanied by a 60% increase in T_1, and a 140% increase in T_2. The results indicate that the percentage changes in T_1 and T_2 taken together can be used to discriminate between areas of inflammation and others which contain demyelination.

FUTURE WORK

1. NMR and EAE in primates

   a) Studies of multiexponential relaxation behaviour *in vivo*.

   b) *In vitro* T_1 and T_2 measurements on normal and abnormal brain tissue. Identification of multiexponential relaxation behaviour of water and fat protons at high field.

   c) *In vitro* NMR spectroscopy on molecules other than water and fat.

   d) High field imaging and spectroscopy *in vivo*

      i) ^{1}H imaging

      ii) ^{31}P imaging

      iii) ^{1}H spectroscopy

      iv) ^{23}Na imaging

   e) Immunological studies on the monkey to correlate them with quantitative measurements, and compare with human data.

2. NMR and MS in Humans

   a) Work has already begun on post mortem NMR studies of brain tissue before and after fixation. Correlations have been made between the NMR images and the gross pathology[57]. Correlations are now being made between the T_1 and T_2 values observed post mortem and after fixation, with the histopathology. The results of

these studies can then be compared with those from the monkey; the ultimate goal being the identification of different types of MS pathology in humans on the NMR image using NMR parameters.

b) Quantitation of NMR parameters *in vivo* and comparison with primate data.

REFERENCES

1. Purcell E.M., Torrey H.C. and Pound R.V. Phys. Rev. 69, 37 (1946).
2. Bloch E., Hansen W.W. and Packard M. Phys. Rev. 70, 474 (1946).
3. Williams D.H. Chem. Soc. Rev., 13(2), 131 (1984).
4. Damadian R. Science 171, 1151 (1971).
5. Moon R.G. and Richards J.H. J. Biol. Chem. 248, 7276 (1973).
6. Henderson T.O., Costello A.J.R. and Omachi A. Proc. Nat. Acad. Sci. USA 71, 2487 (1974).
7. Hoult D.I., Busby S.J.W., Gadian D.G., Radda G.K., Richards R.F. and Seeley P.J. Nature (London) 252, 285 (1974).
8. Dawson M.J., Gadian D.G. and Wilkie D.R. Nature (London) 274, 861 (1978).
9. Nunnally R.L. and Bottomley P.A. Science 211, 177 (1980).
10. Gordon R.E., Hanley P.E., Shaw D., Gadian D.G., Radda G.K., Styles P., Bore P.J. and Chan L. Nature 287, 736 (1980).
11. Alger J.R., Sellerud L.O., Behar K.L., Gillies R.J., Shulman R.G., Gordon R.E., Shaw D. and Hanley P.E. Science 214, 660 (1981).
12. Radda G.K., Bore P.J., Gadian D.G., Ross B.D., Styles

P., Taylor D.J. and Morgan-Hughes J. Nature 295, 608 (1982).

13. Ross B.D., Radda G.K., Gadian D.G., Rocker G., Esiri M. and Falconer-Smith J. N. Engl. J. Med. 304, 1338 (1981).

14. Brenton D.P., Garrod P.J., Krywawich S., Reynolds E.O.R., Bachelard H.S., Cox D.W. and Morris P.G. Lancet I, 115 (1985).

15. Farrar T.C. and Becker E.D. Pulse and Fourier Transform NMR: Introduction to Theory and Methods. New York, Academic Press (1971).

16. Lauterbur P.C. Nature 242, 190 (1973).

17. Bracewell R. The Fourier Transform and Its Applications. New York, McGraw-Hill (1965).

18. Brooks R.A. and Di Chiro G. Phys. Med. Biol. 21, 689 (1976).

19. Kumar A., Welti D. and Ernst R.R. J. Magn. Reson. 18, 69 (1975).

20. Aue W.P., Bartholdi E. and Ernst R.R. J. Chem. Phys. 64, 2229 (1976).

21. Mansfield P.A. and Morris P.G. NMR Imaging in Biomedicine. Ed. Waugh J.S. London: Academic Press (1982).

22. Hinshaw W.S. J. Appl. Phys. 47, 3709 (1976).

23. Hinshaw W.S., Bottomley P.A. and Holland G.N. Nature (London) 270, 722 (1977).

24. Sutherland R.J. and Hutchinson J.M.S. J. Phys. E: Sci. Instr. 11, 79 (1978).

25. Garroway A.N., Grannell P.K. and Mansfield P. J. Phys. C. 7, L457 (1974).

26. Taylor D.G. and Inambar R. In Physical Principles and Clinical Applications of Nuclear Magnetic Resonance. Ed.; Lerski R.A. Paradigm Print, Gateshead. p.23 (1985).

27. Hahn E.L. Phys. Rev. 80, 580 (1950).

28. Carr H.Y. and Purcell E.M. Phys. Rev. 94, 630 (1954).

29. Simmonds D., Banks L.M., Steiner R.E. and Young I.R. Neuroradiology 25, 113 (1983).

30. Young I.R., Bailes D.R., Burl M., Collins A.G., Smith D.T., McDonnell M.J., Orr J.S., Banks L.M., Bydder G.M., Greenspan R.H. and Steiner R.E. J. Comput. Assist. Tomogr. 6, 1 (1982).

31. Herfkens R., Davis P., Crooks L., Kaufman L., Price D., Miller T., Margulis A.R., Watts J., Hoenninger J., Arakawa M. and McRee R. Radiology 141, 211 (1981).

32. Fullerton G.D., Potter J.L. and Dornbluth N.C. Magn. Reson. Imag. 1, 209 (1982).

33. Crooks L.E., Arakawa M., Hoenninger J., McCarten B., Watts J. and Kaufman L. Radiology 151, 127 (1984).

34. Cope F.W. Biophys. J. 9, 303 (1969).

35. Bakker C.J.G. and Vriend J. Phys. Med. Biol. 29(5), 509 (1984).

36. Raine C.S. Lab. Invest. 50(6), 608 (1984).

37. Matthews W.B., Acheson E.D., Batchelor J.R. and Weller R.O. McAlpines' Multiple Sclerosis. London, Churchill Livingstone, Incorporated. (1985).

38. Bailes D.R., Young I.R., Thomas D.J., Straughan K., Bydder G.M. and Steiner R.E. Clin. Radiol. 33, 395 (1982).

39. Young I.R., Hall A.S., Pallis C.A., Bydder G.M., Legg N.J. and Steiner R.E. Lancet II, 1063 (1981).

40. Levy G.C. and Peat I.R. J. Magn. Reson. 18, 500 (1975).

41. Stewart W.A. and Hall L.D. Phys. Med. Biol. In press.

42. Fukushima E. and Roeder S. Experimental Pulse NMR: A Nuts and Bolts Approach. Addison-Wesley, Massachusetts. p.48 (1981).

43. Abragam A. The Principles of Nuclear Magnetism. Eds.; Marshall W.C. and Wilkinson D.H. Oxford University Press (1961).

44. Dwek R.A. Nuclear Magnetic Resonance (NMR) in Biochemistry: Applications to Enzyme Systems. Eds.; Harrington W. and Peacocke R. Oxford University Press, p.175 (1973).

45. Ibid. p.177.

46. Lynch L.J. and Webster D.S. J. Magn. Reson. 40, 259 (1980).

47. Freeman R. and Hill L.D.W. J. Chem. Phys. 54(8), 3367

(1971).

48. McDonald G.G. and Leigh J.S. Jr. J. Magn. Reson. 9, 358 (1973).
49. Hanssum H. J. Magn. Reson. 45, 461 (1981).
50. Sass M. and Ziessow D. J. Magn. Reson. 25, 263 (1977).
51. Pykett I.L., Rosen B.R., Buonanno F.S. and Brady T.J. Phys. Med. Biol. 28(6), 723 (1983).
52. Rosen B.R., Pykett I.L. and Brady T.J. J. Comput. Assist. Tomogr. 8(2), 195 (1984).
53. Meiboom S. and Gill D. Rev. Sci. Instrum. 29, 688 (1958).
54. Alvord E.C., Shaw C. and Hruby S. Ann. Neurol. 6, 469 (1979).
55. Alvord E.C., Shaw C.M., Hruby S., Sires L.R. and Slimp J.C. In Experimental Allergic Encephalomyelitis: A Useful Model for Multiple Sclerosis. Eds.; Alvord E.C., Kies M.W. and Suckling A.J. New York, Alan R. Liss, Incorporated. p.461 (1984).
56. Stewart W.A., Alvord E.C., Hruby S., Hall L.D. and Paty D.W. Lancet. II, 898 (1985).
57. Stewart W.A., Berry K., Hall L.D. and Paty D.W. Lancet II, 412 (1984).

APPENDIX I

Block Diagram of Picker International Imaging Instrument